PD AL 0702

Pattern Synthesis Studies for Planar and Non-Planar Conformal Arrays

HEMA SINGH, B S KAVITHA LEKSHMI, D POOVANNAN, R M JHA
Aerospace Electronics & Systems Division

Project Document AL 0702
March 2007

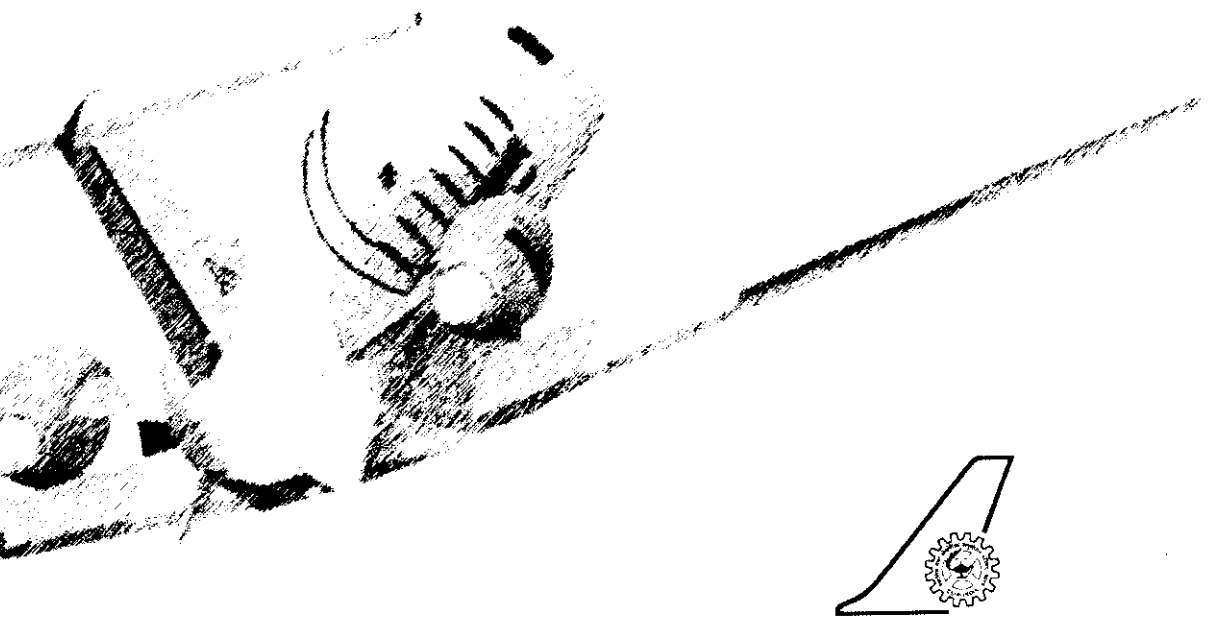

National Aerospace Laboratories
Bangalore 560 017, India

Contents

Pattern Synthesis Studies for Planar and Non-planar Conformal Arrays

1. Introduction

Phased array antennas are being used in various fields, *viz.* radio and microwave communication, radio astronomy, space and terrestrial telecommunications. Irrespective of the spatial distribution of the antenna elements, beam of phased array can be steered by the phase variations along the array. The maximum gain can be achieved depending on the array configuration. However these antenna arrays have limited angular range of scanning. Further for small platforms such as unmanned aerial vehicles (UAV) and fighter aircraft, phased array antenna having high directivity cannot be mounted because of their large size and weight. Conformal arrays, one of the general types of phased arrays offer a possible solution to these problems. Conformal array antenna assumes the shape of the structure/platform, *viz.* aircraft, missiles, ships. They generally belong to the class of non-linear arrays.

A modern concept for the use of conformal array is termed as *smart skin*, in which the surface of a platform is covered with antenna elements forming an array (Drabowitch *et al.* 2005). Conformal arrays offer several advantages over the conventional phased arrays that includes the following:

1. Since the antenna elements are mounted along the surface, there is no aerodynamic drag. In other words, conformal array provide aerodynamic shape compatible with the corresponding platform.
2. The conformal design yields potentially greater effective aperture for the same class of platform.
3. Payload weight gets reduced. No rigid support of radome is necessary. Furthermore the error in scan angle that occurs with a radome in a linear or planar array is eliminated or reduced.
4. A conformal antenna design can provide 360° coverage without any mechanical rotation of antenna array.
5. The signal environment of the antennas is, in general, very complex. It consists of multiple desired signals coming from various directions with different frequencies and polarizations along with natural or deliberate interfering signals (jammers/ hostile

sources), multipath, etc. Conformal arrays offer improved flexibility while extracting the useful information.

In general, conformal array have non-uniform element spacing and a non-planar shape due to which many complications arise such as

1. The loss of certain desirable beam pattern characteristics.
2. Since the array is three-dimensional it may be difficult to ensure that all the elements radiate the same polarization. One may suggest to use circular polarization, but it is difficult to obtain an element pattern that remains perfectly circularly polarized over a wide range.
3. A non-uniform magnitude of the spatial steering vector.
4. It is difficult to etch elements on singly- or doubly- curved surfaces.

Such complications can severely degrade the performance of the antenna array. This opens a novel area of interest for the researchers. In the present report, simulation study for the pattern synthesis of circular aperture, circular arrays, hexagonal arrays and cylindrical arrays is carried out. Simulated results are validated against the literature. Starting form the most basic continuous circular aperture, pattern is synthesized using different excitations (Section 2). Simulations are then extended for the circular aperture with discrete antenna elements (Section 3) excited with different amplitude distributions, *viz*. Taylor, Dolph-Chebyshev and Villeneuve weighting. The concept of phase mode excitations is employed for the generation of the beam pattern. In Sections 4 and 5, pattern synthesis of circular sector arrays and the hexagonal arrays respectively is presented. Section 6 consists of simulations on cylindrical arrays excited with the Dolph-Chebyshev and Villeneuve weightings.

2. Continuous Circular Aperture

Circular and cylindrical arrays are used in applications that require coverage over the full 360° of azimuth with little variation of sidelobe level or beamwidth. They have potential of usage w.r.t. operation over wide bandwidths. The circular arrays are preferred choice for direction finding applications. This is due to the wide-spaced elements that give a high sensitivity of differential phase-to-signal direction. However they are found to be not so good for forming low sidelobe beams.

The basic symmetry of circular arrays offers several advantages, which in addition to 360° scan angle, include an ability to compensate for the effects of mutual coupling by segregating the array excitation into a series of symmetrical spatial components. Further its directional patterns remain constant in shape over broad bandwidth. Other circular array applications include Wullenweber arrays for direction finding, wide bandwidth communication arrays, wrap-around antennas for shipborne communications, spacecraft antennas, and null-steering antennas for mobile communications.

For one-dimensional (or linear) apertures, the uniform distribution and the Taylor equal-sidelobe distribution are widely used. The uniform aperture of length L produces $(\sin\pi u)/\pi u$ pattern, where $u=(L/\lambda)\sin\theta$, with 13.26 dB sidelobe ratio. The wavelength λ and the angle θ are measured from broadside.

2.1 Uniform Weighting

The circular antenna arrays are excited so as to arrange the signals from all the elements to add together in phase for a single mainbeam direction. The circular apertures (Fig. 2.1) provide the limiting case for most of the array configurations such as the concentric circular array, hexagonal arrays etc.

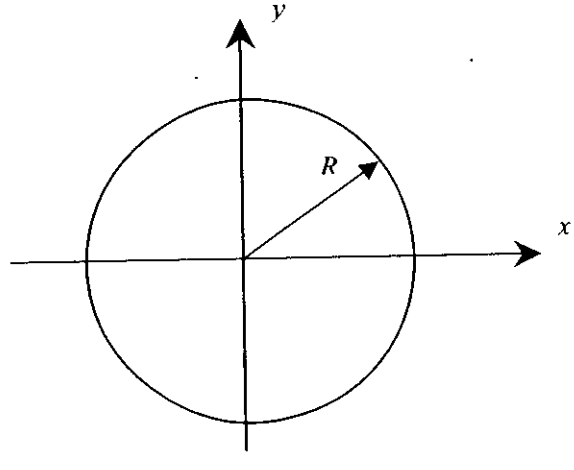

Figure 2.1 Geometry of a circular aperture of radius R.

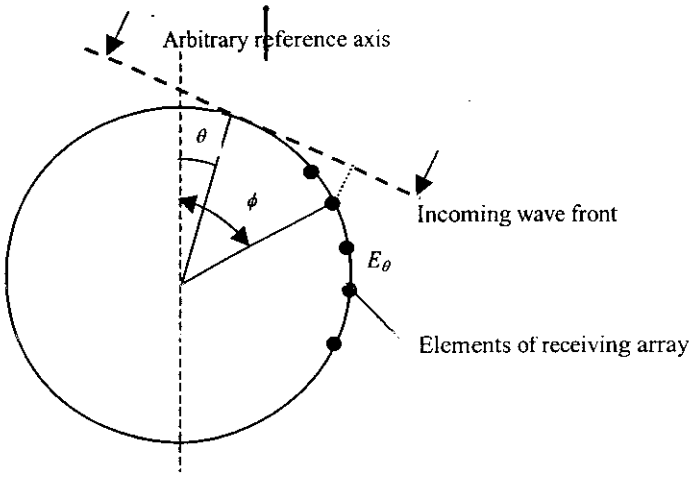

Figure 2.2 Wave front arriving at circular array from direction θ.

Assuming the mainbeam direction at θ=0°, the excitation at angle ϕ around the array of radius r (Fig. 2.2) is given by

$$F(\phi) = \exp\left(-j\frac{2\pi r}{\lambda}\cos\phi\right) \tag{2.1}$$

For a circular array with isotropic elements and very small inter-element spacing, the normalized pattern (Rudge *et al.* 1983) in the elevation plane is expressed as

$$D(\theta) = \frac{1}{2\pi}\int_0^{2\pi} F(\phi)\exp j\left(\frac{2\pi r}{\lambda}\cos(\phi-\theta)\right)d\phi \tag{2.2}$$

Thus,

$$D(\theta) = J_0\left(\frac{4\pi r}{\lambda}\sin\frac{\theta}{2}\right) \tag{2.3}$$

where, $D(\theta)$ is the directional pattern, $J_o(x)$ is the zero order Bessel function, θ is the angle measured with respect to the horizontal axis and λ is the free-space wavelength.

Figure 2.3 shows the azimuth plane pattern of a phase-compensated circular array having a continuous aperture distribution with no amplitude tapering. The diameter of array is taken to be 5λ. The computed results are validated against those available in literature (Rudge *et al.* 1983). It can be observed that the pattern consists of high near-in sidelobes (-9 dB). The beamwidth of the mainlobe is narrow as compared to a corresponding linear array of length equal to the diameter of the circle (Fig. 2.4). The reduced beamwidth and multiple sidelobes are due to increased concentration of the elements at the sides of the circular aperture as compared to a linear array. The low sidelobes can be obtained by means of symmetrical amplitude taper on the front half of the circular array with zero or low excitation on the back

of the array (James 1965). Beam steering of this pattern can be achieved by electronic control of both amplitude and phase of each element.

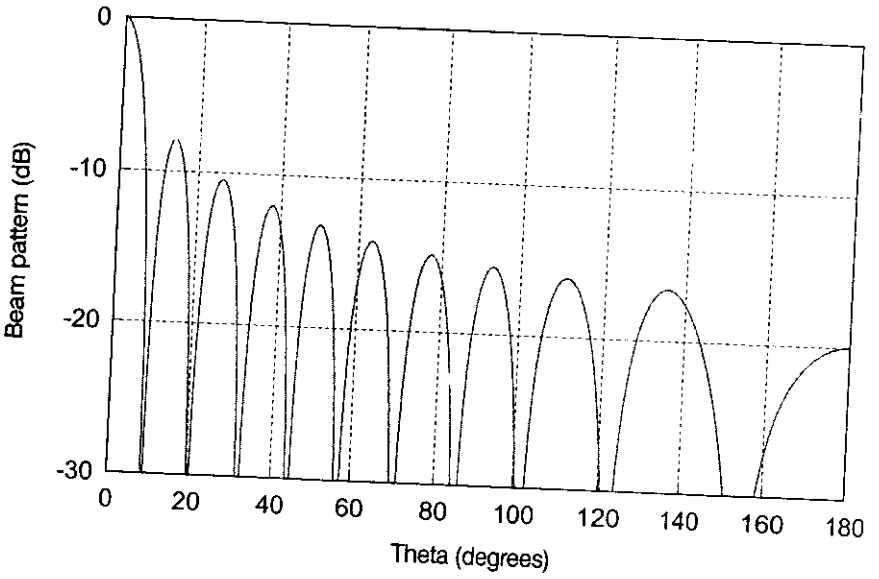

(a)

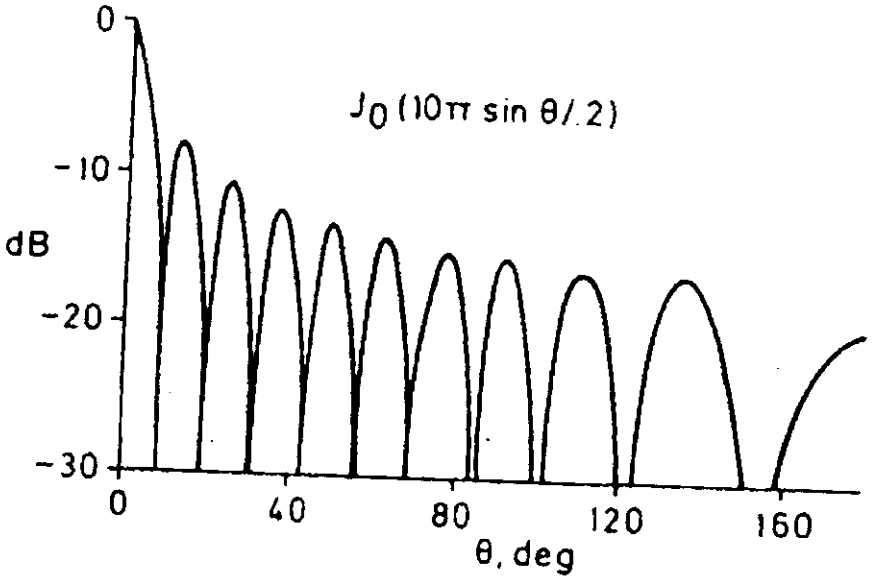

(b)

Figure 2.3 Validation plot for *azimuth plane pattern* of a phase-compensated circular array of diameter of 5λ; *a continuous aperture distribution with no amplitude tapering.* (a) Computed plot (b) Reference plot (Rudge *et al.* 1983)

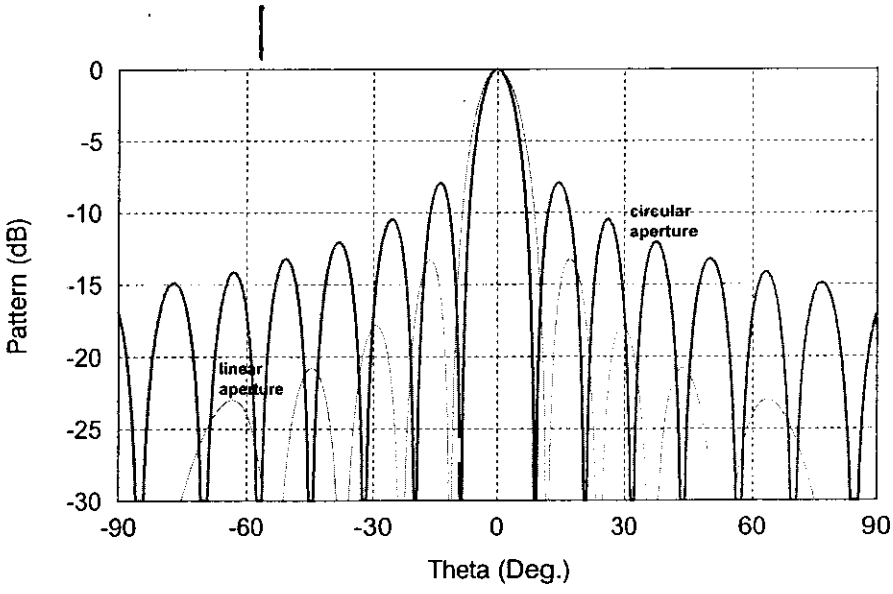

Figure 2.4 Comparison of beam pattern of linear array and circular array with continuous distribution. The length of linear array is equal to the diameter of the circular array (5λ).

The corresponding elevation plane pattern (Fig. 2.5) is given by

$$D(\alpha) = J_0\left[\frac{2\pi r}{\lambda}(1-\cos\alpha)\right] \tag{2.4}$$

where, $D(\alpha)$ is the beam pattern in vertical plane and α is the angle in the vertical plane. The computed results are validated against the literature (Rudge *et al.* 1983). It can be observed that the beamwidth in elevation plane is large. Since this is equivalent to *end-fire* position for a linear array. This provides wideband performance, as the mainbeam is a function of $J_o(x)$, which is not a function of frequency. Moreover this demonstrates that single ring circular arrays provides a fan beam for 360° coverage and thus have application in surveillance radar. However one cannot have independent control of the horizontal and vertical beamwidths. If amplitude tapering is incorporated for achieving low sidelobes in the horizontal plane, the vertical plane pattern will have broader beam. However in both the planes the sidelobes decay monotonically.

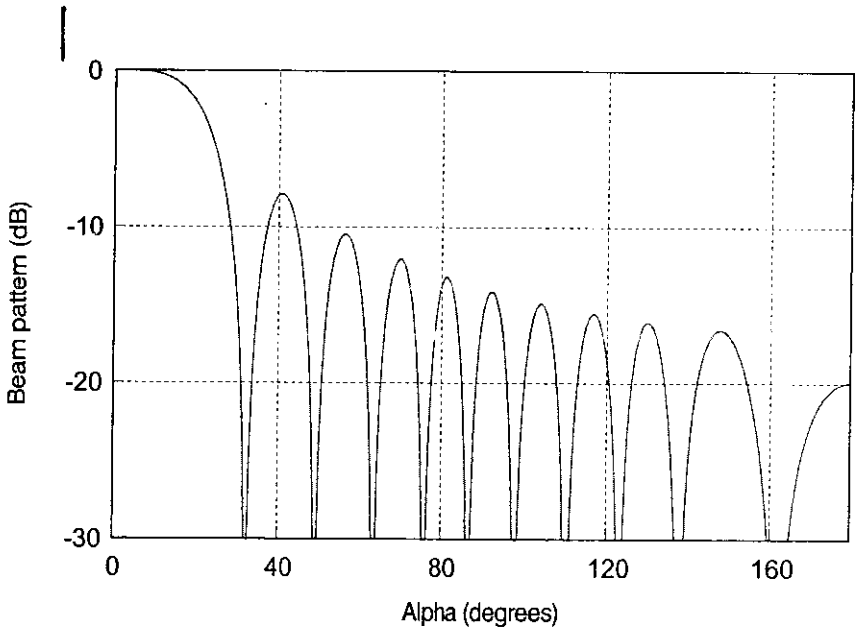

(a)

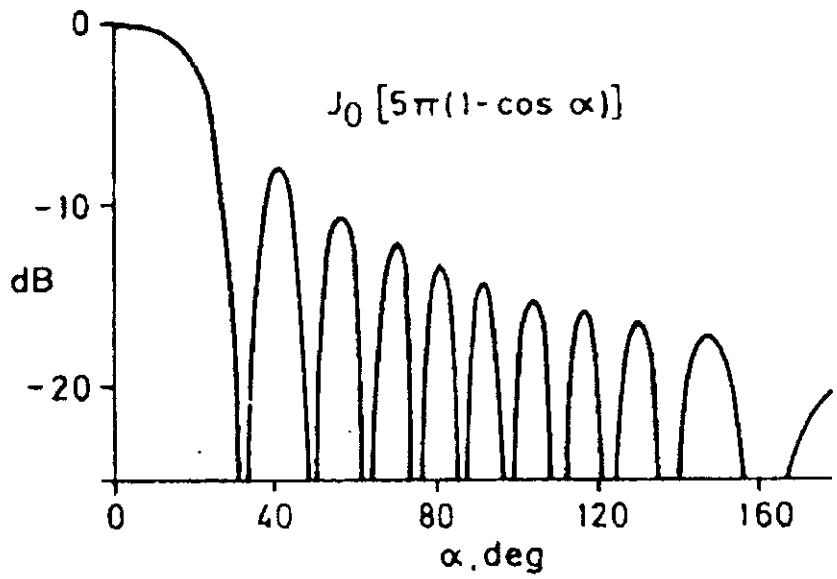

(b)

Figure 2.5 Validation plot for *elevation plane pattern* of a phase-compensated circular array of a diameter of 5λ; *a continuous aperture distribution with no amplitude tapering.* (a) Computed plot (b) Reference plot (Rudge *et al.* 1983)

Figure 2.6 represents the normalized beam pattern of the circular aperture in *xy*-plane for $R/\lambda = 10$. The pattern is synthesized with uniform weighting. The beam pattern (Trees 2002) is given as $B(\theta) = 2\frac{J_1(\pi u_R)}{\pi u_R}$ (2.5)

where, $u_R = \frac{2R}{\lambda}\sin\theta$ and R is the radius of circular aperture. Since u_R contains a factor of R, the visible region is $0 \leq u_R \leq 2R/\lambda$. Using $u_R = \Psi_R/\pi$, the visible region can be written as $0 \leq \psi_R \leq 2\pi R/\lambda$.

The simulated results are validated against the literature (Trees 2002). It can be observed that height of first sidelobe is –17.6 dB (approx.). On comparison with a square aperture of the same area, the circular aperture has a slightly larger 3-dB beamwidth, but the sidelobes are significantly lower (-17.6 dB versus –13.4 dB).

2.2 Taylor Weighting

Taylor (1960) developed a procedure for the pattern synthesis of a circular aperture. It is a slight modification of the method used for line sources. The Taylor distribution has a pattern in which all the sidelobes are of equal level (Taylor ideal line source) or in which $\bar{n}$ sidelobes are of equal level (Taylor approximate line source), $\bar{n}$ being the transition index. The Taylor pattern is the continuous equivalent of the discrete Dolph-Chebyshev array distribution. It offers the narrowest possible beamwidth for a given sidelobe ratio.

Relating a parameter H in terms of sidelobe ratio, SLR = $17.57 + 20 \log \frac{2I_1(\pi H)}{\pi H}$, the Taylor pattern for circular aperture (Hansen 1976) can be obtained as

$$F(u) = \frac{2J_1\left(\pi\sqrt{u^2 - H^2}\right)}{\pi\sqrt{u^2 - H^2}} \qquad \text{for } u \geq H \tag{2.6}$$

$$F(u) = \frac{2I_1\left(\pi\sqrt{H^2 - u^2}\right)}{\pi\sqrt{H^2 - u^2}} \qquad \text{for } u \leq H \tag{2.7}$$

where, J_1 and I_1 are the Bessel and the modified Bessel functions of the first kind and order one.

Figure 2.7 describes the Taylor pattern for a circular aperture of aperture length 10λ and sidelobe ratio of –30 dB. Here the value of H is taken as 1.1977 for SLR corresponding to 30 dB. The computed plot is validated against those available in open literature (Hansen 1976).

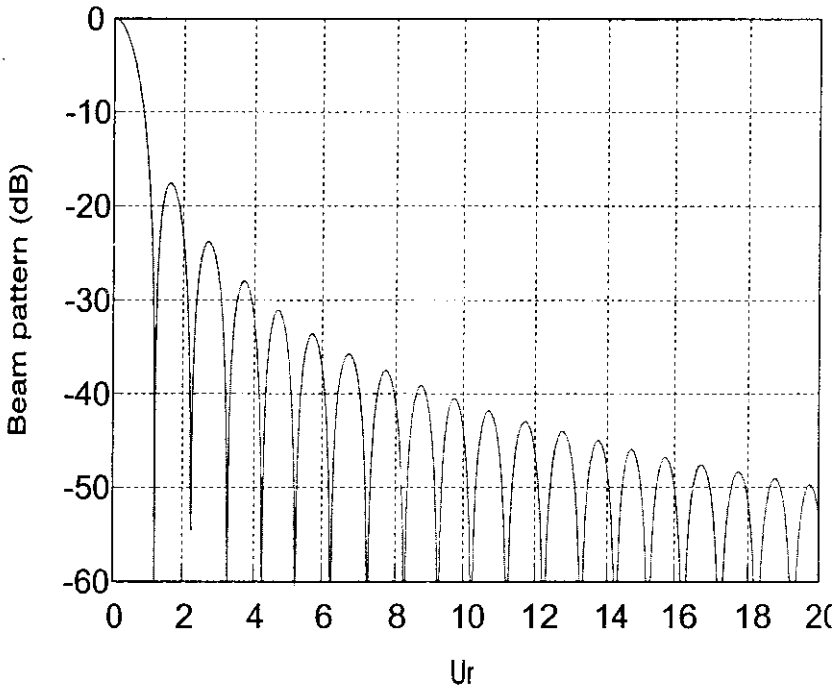

(a)

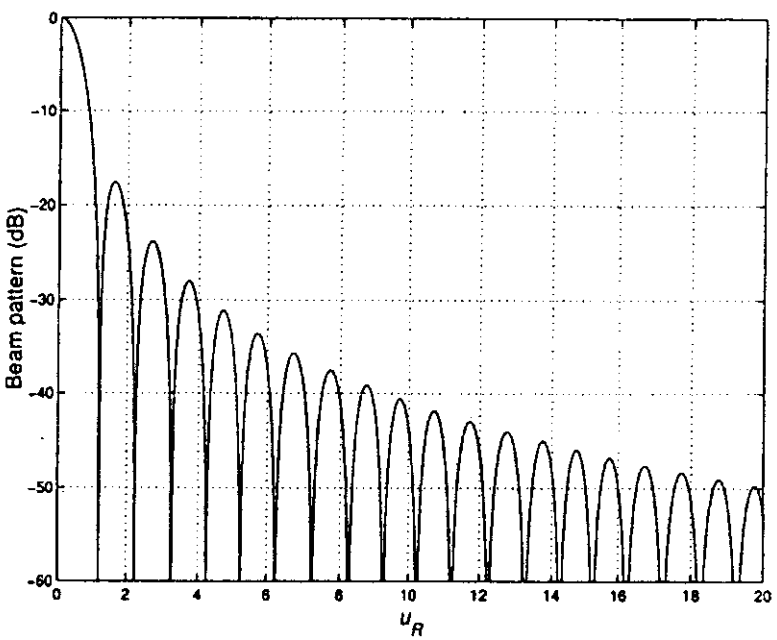

(b)

Figure 2.6 Validation plot for beam pattern of a *circular aperture* with radius of $R/\lambda = 10$; $0 \leq u \leq 2R/$ The *uniform distribution* is employed. (a) Computed plot (b) Reference plot (Trees 2002).

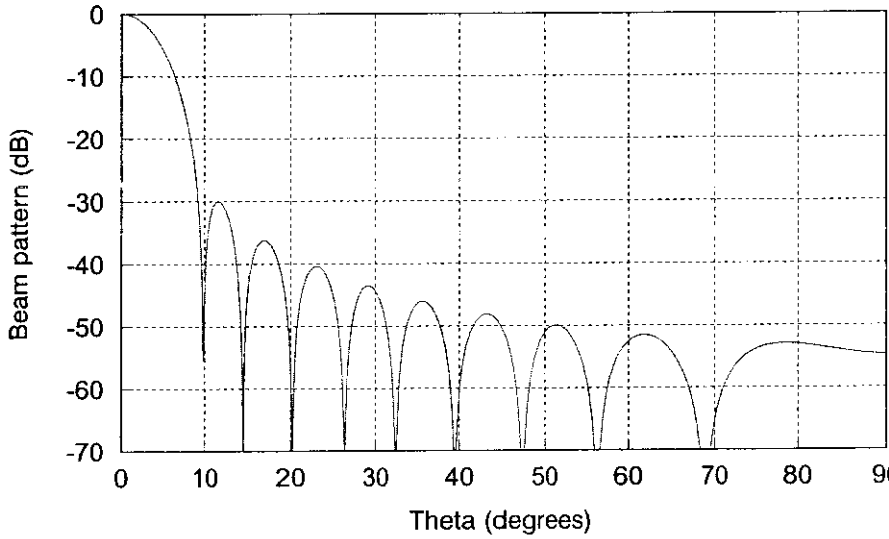

(a)

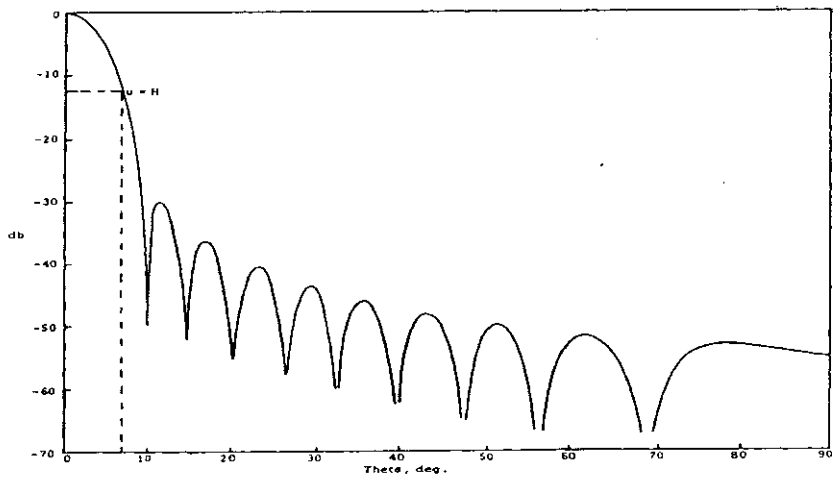

(b)

Figure 2.7 Validation plot of *Taylor pattern* for a *circular aperture* of length 10λ and sidelobe ratio -30 dB. (a) Computed plot (b) Reference plot (Hansen 1976).

3. Circular Arrays

A circular array consists of equally spaced N-elements placed in a circular ring (Fig. 3.1). It is of particular importance because it is also a basic element of cylindrical arrays and even conical and spherical arrays, or arrays on generalized bodies of revolution.

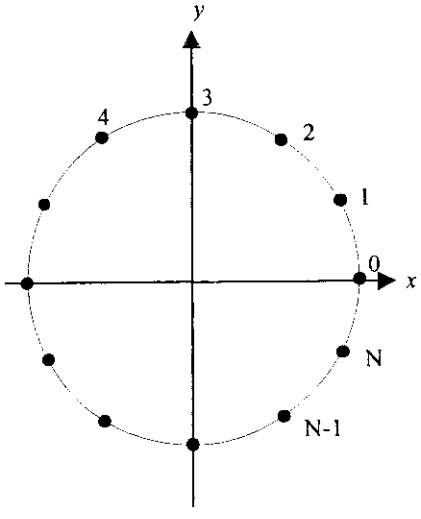

Figure 3.1 Geometry of a circular array.

For a circular array with isotropic elements, the array weighting corresponds to the sampling of continuous aperture weighting. For the generation of the M spatial harmonics, the number of the elements, according to the sampling theorem, should be $N \geq 2\left(\frac{2\pi R}{\lambda}\right)+1$, where R is the radius of the circular aperture. This implies that the spacing between the elements on the arc is $d \leq \frac{\lambda}{2}$.

The pattern characteristics of circular and cylindrical arrays cannot be expressed as the product of an element pattern and the array factor. This necessitates the consideration of the array patterns with directional elements. Moreover the mutual coupling between the elements narrows the element pattern, so in practice, omnidirectional elements cannot be designed. Although it is true for planar arrays, it is much more important in conformal arrays. This is because all the elements in conformal arrays point in different directions. The interaction between widely separated omnidirectional elements results in narrowed pattern and very limited bandwidth. Thus, if the array is designed using elements that radiate primarily in the radial direction, or in some forward sector, the characteristics of circular array will be substantially different and the bandwidth will also be improved (Mailloux 2005).

3.1 Circular Arrays with Uniform Excitation

The beam pattern (Trees 2002) of the circular array with uniform distribution is given by

$$B(\theta,\phi)=\sum_{n=0}^{N-1}\omega_n \exp[jk_0R\sin\theta\cos(\phi-\phi_n)+j\beta_n] \tag{3.1}$$

where β_n is the phase factor with respect to the origin, expressed as

$$\beta_n = -k_0R\sin\theta_0\cos(\phi_0-\phi_n) \tag{3.2}$$

If the main response axis is steered, it is convenient to define new set of variables. Thus, rewriting eq(3.1), we have

$$B(\theta,\phi)=\sum_{n=1}^{N}\omega_n \exp[jk_0\rho\cos(\xi-\phi_n)] \tag{3.3}$$

where, $\rho = R\left[(\sin\theta\cos\phi-\sin\theta_0\cos\phi_0)^2+(\sin\theta\cos\phi-\sin\theta_0\cos\phi_0)^2\right]^{\frac{1}{2}}$

$$\cos\xi = \frac{\sin\theta\cos\phi-\sin\theta_0\cos\phi_0}{\left[(\sin\theta\cos\phi-\sin\theta_0\cos\phi_0)^2+(\sin\theta\sin\phi-\sin\theta_0\sin\phi_0)^2\right]^{\frac{1}{2}}}$$

For uniform excitation and equally spaced elements, $\omega_n=\frac{1}{N}$ and $\phi_n=\frac{2\pi n}{N}$.

The resulting beam pattern is

$$B(\theta,\phi)=\sum_{m=-\infty}^{\infty} j^{mN}e^{-jmN\xi}J_{mN}(k_0\rho) \tag{3.4}$$

The beam pattern of a uniform circular array with $2\pi R_\lambda$=10 for the θ_o=0 is shown in Fig. 3.2. Two cases, *viz.* $\phi=0$ and $\phi=\frac{\pi}{2}$ are considered. Thus the beam patterns reduces to

$$B(\theta,\phi)=\sum_{m=-\infty}^{\infty} j^{mN}e^{-jmN\xi}J_{mN}(k_0R\sin\theta) \tag{3.5}$$

The number of elements in an array is varied (N =10, 20, 25) and the resulting pattern is obtained. Figure 3.3 shows the beam pattern for a uniform circular array steered to broadside, i.e. for $\phi=\frac{\pi}{2}$ or $\frac{3\pi}{2}$. It also consists of the beam patterns for N = 10, 20, 25 antenna elements. It is observed that the mainlobe width is not affected by increasing the number of elements in circular array. The computed plots are validated against those available in open literature (Trees 2002).

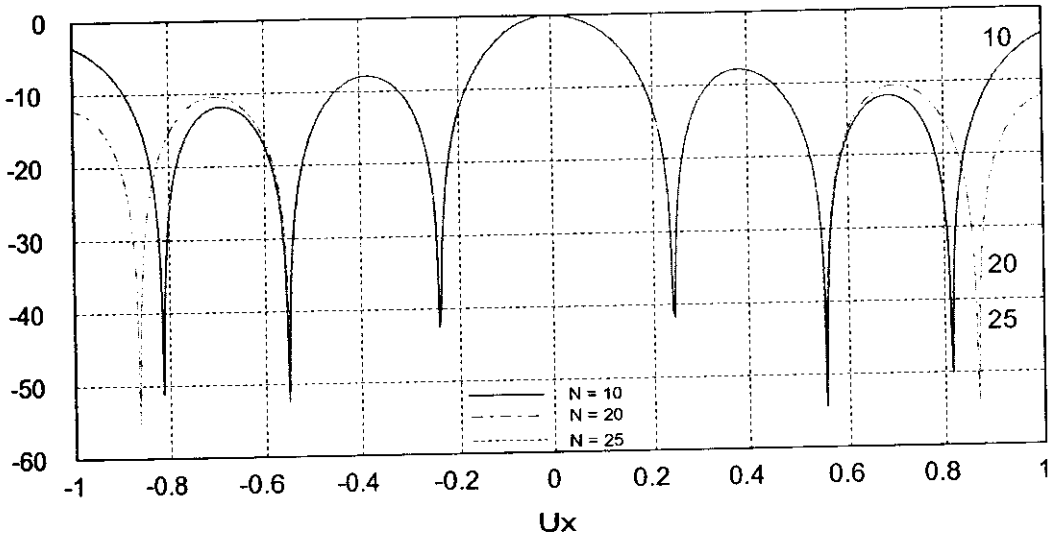

(a)

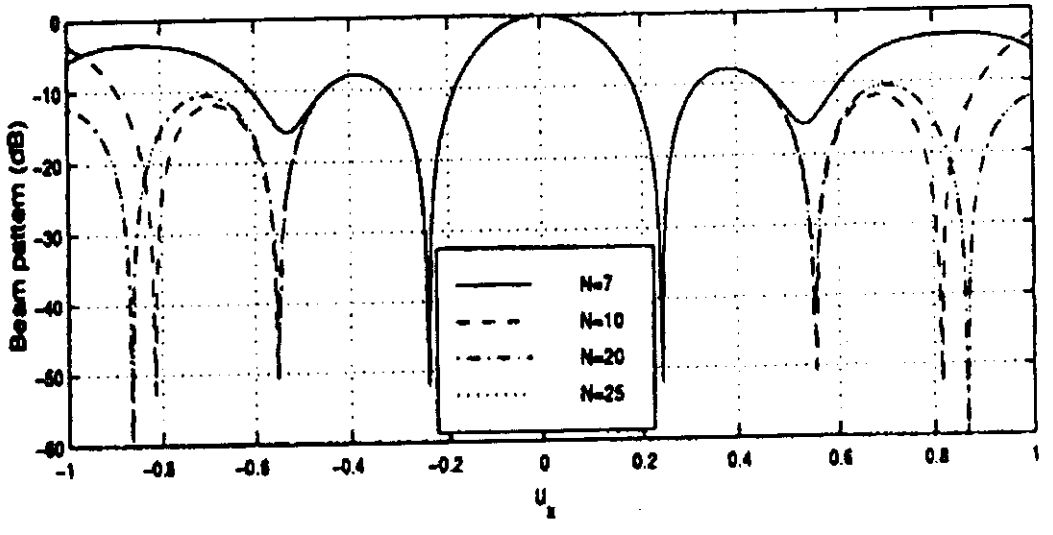

(b)

Figure 3.2 Validation plot for beam patterns of *uniformly excited circular array steered to broadside*; ϕ = 0 and π with N = 10, 20, 25. (a) Computed plot (b) Reference plot (Trees 2002).

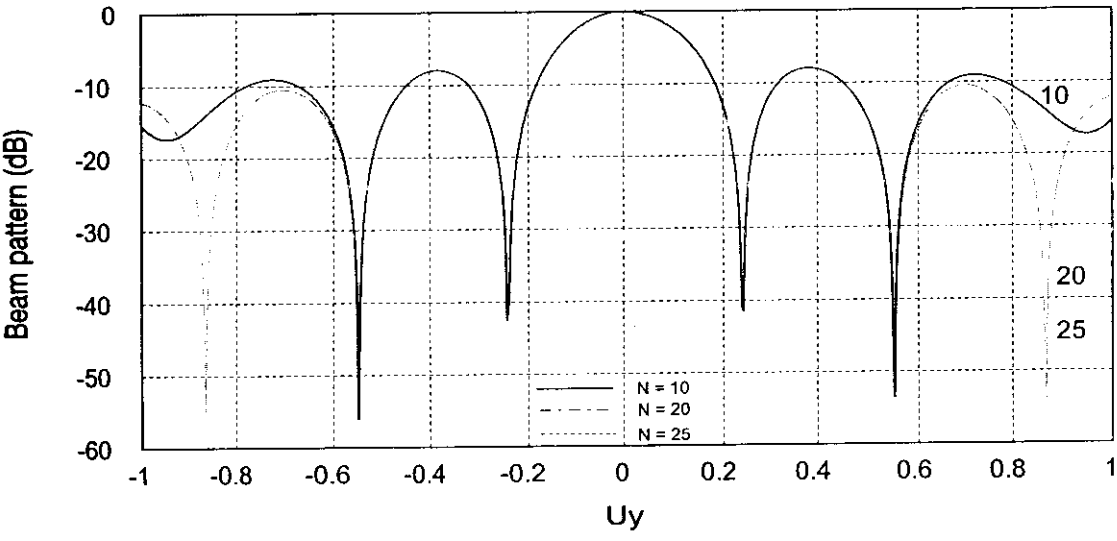

(a)

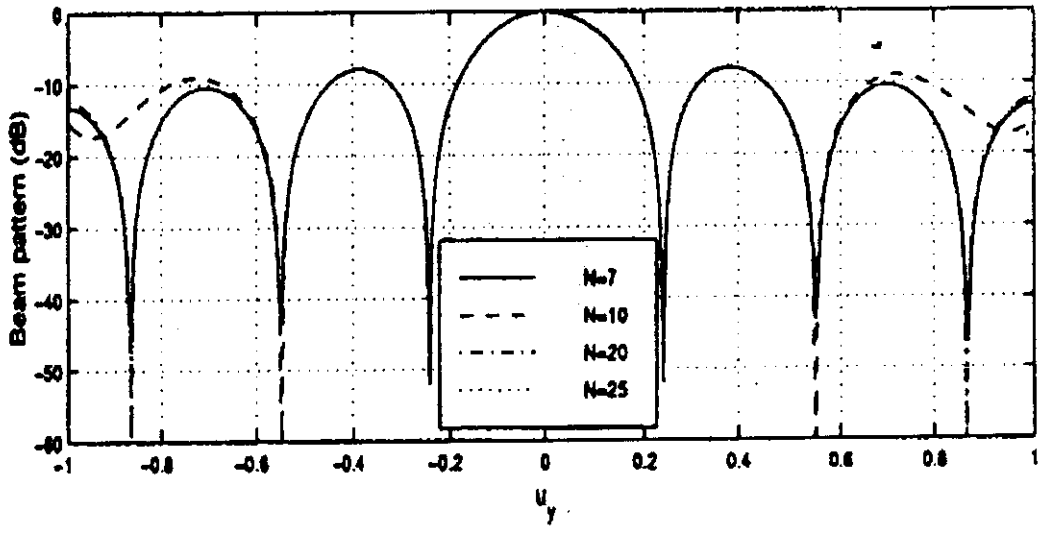

(b)

Figure 3.3 Validation plot for beam patterns of *uniformly excited circular array steered to broadside;* $\phi = \pi/2$ and $3\pi/2$ with N = 10, 20, 25. (a) Computed plot (b) Reference plot (Trees 2002).

3.2 Phase Mode Excitation in Circular Arrays

In circular arrays, omnidirectional patterns are often synthesized in terms of a spatially orthogonal set of phase modes. Davies (1965) showed that phase modes may be treated in the same way as the elements of a uniformly spaced linear array, and all the techniques developed for linear array pattern synthesis may be applied to the circular array subject to the comments as follows:

1. Phase modes are omnidirectional in azimuth, so the elements are also omnidirectional. The radiation pattern of the circular array corresponds to the array factor of the linear array.
2. Phase modes are orthogonal (since they are the outputs of a discrete Fourier Transform), so there is no mutual coupling.
3. The radiation patterns have the same shape (in θ-space) as those formed by a linear array (in $kd\sin\theta$-space) with an inter-element spacing of half-wavelength, independent of frequency.

A far-field nth-order phase mode pattern is defined as having constant amplitude and a phase varying linearly from 0 to $2n\pi$. The nth-order phase mode may be generated in the far field by exciting a corresponding nth-order current phase mode on the array.

In the Butler-matrix-fed circular array, the beam is scanned through 360° by changing only the phases of the matrix input currents. The Butler matrix inputs are used to feed the antenna elements forming a narrow radiated beam. This beam can be scanned usually like the linear array beam by the operation of phase shifters alone.

The operation of this multimode array can be described in terms of phase modes (Drabowitch *et al.* 2005). This involves the distribution of currents impressed on the radiating elements by the matrix. However the radiation pattern of the multimode array varies as it is scanned continuously rather than in discrete steps. For continuous scanning of a multimode array, the mode amplitudes are held constant and a linear phase progression is set up on the mode inputs by operating the variable phase shifters. All these modes have far-field patterns. In an N-element array the highest order mode ($K=N/2$) has an element-to-element phase variation of π radians. For example, in the array of the dipole elements around a cylinder, the mode pattern is obtained by summing different number of modes.

Let us consider a continuous circular array (i.e. one with an infinite number of omnidirectional elements and negligible inter-element spacing). The excitation of an array F

can be taken as a periodic function of azimuth angle θ, of period 2π, and can be expressed as a Fourier series

$$F(\theta) = \sum_{m=-N}^{N} C_m \exp(jm\theta) \tag{3.6}$$

Each term of the series is known as a phase mode, and C_m is the corresponding phase mode coefficient. It can be seen that a zero-order phase mode (m=0) corresponds to an excitation of constant phase as a function of azimuth angle. The first order phase mode (m=1) corresponds to one cycle of phase over 360° of azimuth. The negative-order phase modes simply correspond to the phase variation in the opposite sense.

When an array is excited by a single phase mode, the far-field pattern $D_m(\theta)$ will be

$$D_m(\theta) = C_m j^m J_m(k_o r) \exp(jm\theta) \tag{3.7}$$

The far-field phase modes are omnidirectional in azimuth, but each having the characteristic variation of phase with azimuth angle similar to the corresponding excitation phase mode.

When a discrete array is analyzed, the same theory applies, but the excitation function $F(\theta)$ is sampled at the element locations by a sampling function $S(\theta)$. For an n omnidirectional elements

$$S(\theta) = \sum_{q=-\infty}^{\infty} \exp(jnq\theta) = 1 + \sum_{q=1}^{\infty} \exp(jnq\theta) + \sum_{q=-\infty}^{-1} \exp(jnq\theta) \tag{3.8}$$

giving

$$D_m(\theta) = C_m j^m J_m(k_o r) \exp(jm\theta) + \sum_{q=1}^{\infty} C_m j^{-g} J_{-g}(k_o r) \exp(-jg\theta) + \sum_{q=-\infty}^{-1} C_m j^h J_h(k_o r) \exp(-jh\theta) \tag{3.9}$$

where g=(nq-m) and h=(nq+m).

The first term is identical to that for a continuous array. The two series terms represent ripple terms as a function of θ. As a rule of thumb, the inter-element spacing should be no greater than half-wavelength in order to keep the spatial ripple acceptably low. For an N-element array, it is possible to have N+1 phase modes, though the $+N/2$ and $-N/2$ phase modes are actually identical. The discrete Fourier Transform to generate the phase modes from the element signals is conveniently provided by a Butler matrix. A plane wave incident on the array will excite all the phase modes simultaneously.

Let us consider a circular array of radius R with N elements equally spaced at $\alpha_J = \frac{2\pi J}{N}$, where J=1, 2, ...N. The radiation pattern of the array (Sheleg 1968) is given by

$$E(\phi) = \sum_{J=1}^{N}\left[\sum_{K} B_K e^{j\beta_K} e^{jJK(2\pi/N)}\right] A(\phi - \alpha_J) e^{j(2\pi R/\lambda)\cos(\phi-\alpha_J)} \tag{3.10}$$

The approximate pattern of the dipole in front of a cylinder is

$$A(\phi) = \frac{1}{2}(1 + \cos\phi) \tag{3.11}$$

The mode amplitudes B_K are held constant (B_K = 1) and with phases corresponding to those in Table 3.1.

TABLE 3.1

The phases of the pattern modes of a 32-element array (Sheleg 1968)

Mode	Relative Gain (in dB)	Relative Phase at $\phi = 0$ (in degrees)
0	0.0	0.00
1	0.2	0.74
2	0.1	7.51
3	0.2	14.63
4	0.2	29.27
5	0.0	44.63
6	0.5	63.06
7	0.2	91.93
8	-0.5	115.35
9	0.8	144.56
10	1.0	-168.45
11	-0.5	-128.07
12	0.7	-105.74
13	3.5	-35.18
14	5.1	20.91
15	5.6	120.92
16	5.6	-172.05

Figures 3.4 illustrate the mode-by-mode build-up of the pattern of a 32-element array with uniform excitation of the modes. The spacing between elements is considered as 0.5λ. The results are shown for the modes corresponding to $K = 0, \pm 1, \pm 2, \ldots\ldots, \pm 15$. It can be seen that the beam narrows as more modes are added and until ± 11 modes are reached, the far-out sidelobes decrease as if the modes are perfect.

As already mentioned, the multimode array involves the continuous distribution of current. The radiation pattern is the sum of the modes contribution made to the pattern of a circular array by its elements. The resultant pattern of a continuous current sheet is expressed as,

$$E(\phi) = \frac{\sin\left[\frac{2N+1}{2}(\phi - \phi_0)\right]}{\sin\left(\frac{\phi - \phi_0}{2}\right)} \tag{3.12}$$

where, ϕ is the angle off-broadside and ϕ_o is the phase difference between adjacent modes.

Figure 3.5 shows the comparison of the patterns of a 32-element circular array and of continuous current sheet using 21 modes (± 10 modes) with uniform distribution $B_K = 1$ and the phases corresponding to Table 3.1. The computed results are validated against those available in literature (Sheleg 1968). Figure 3.6 demonstrates the similar comparison for 31 modes (± 15 modes). It is apparent that the patterns for discrete and continuous cases agree within 0.5 dB.

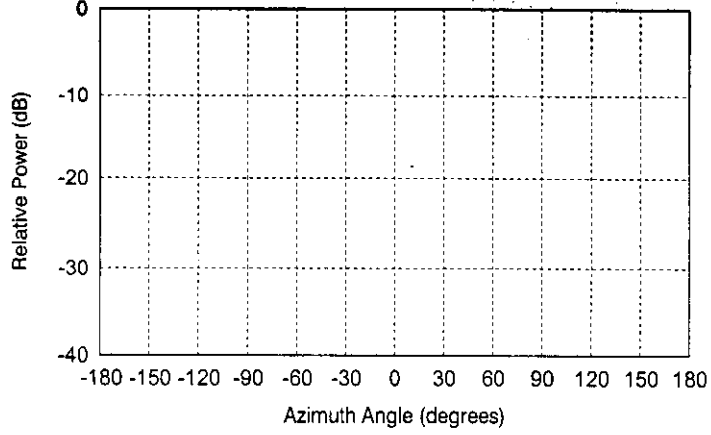

(a)

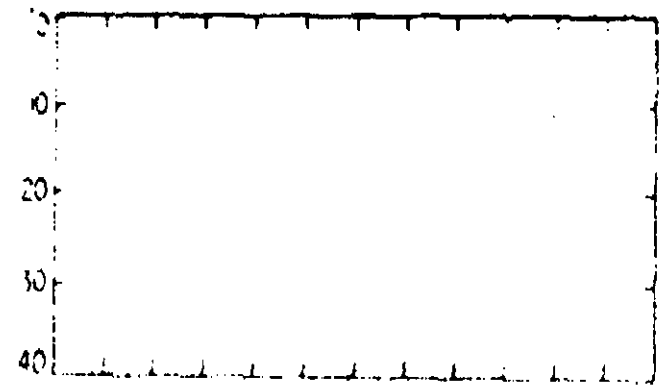

(b)

(i) Mode 0 (Figure text given on page 26)

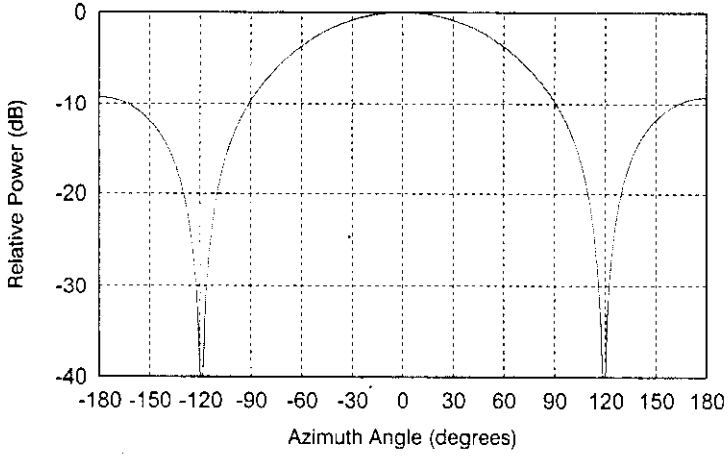

(a)

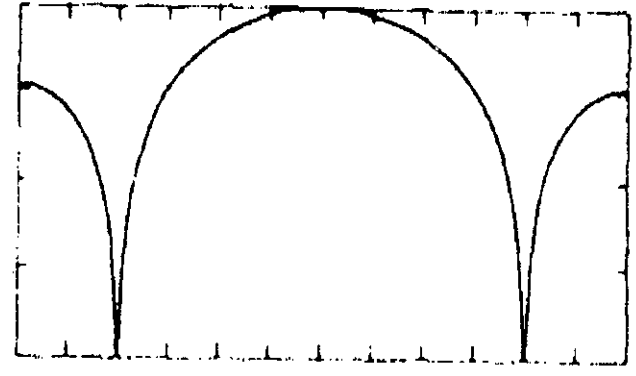

(b)

(ii) Mode –1 through +1 (Figure text given on page 26)

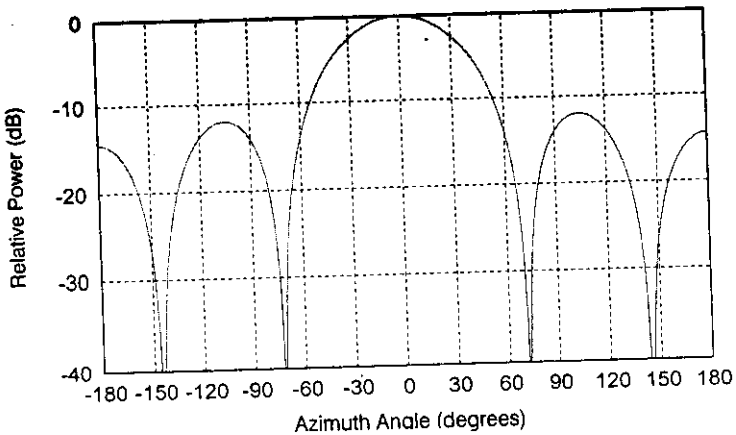

(a)

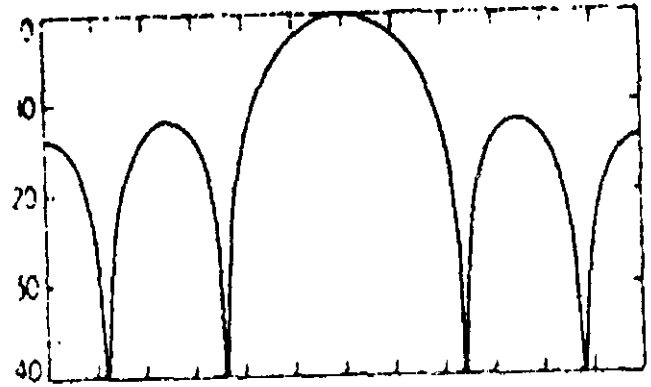

(b)

(iii) Mode –2 through +2 (Figure text given on page 26)

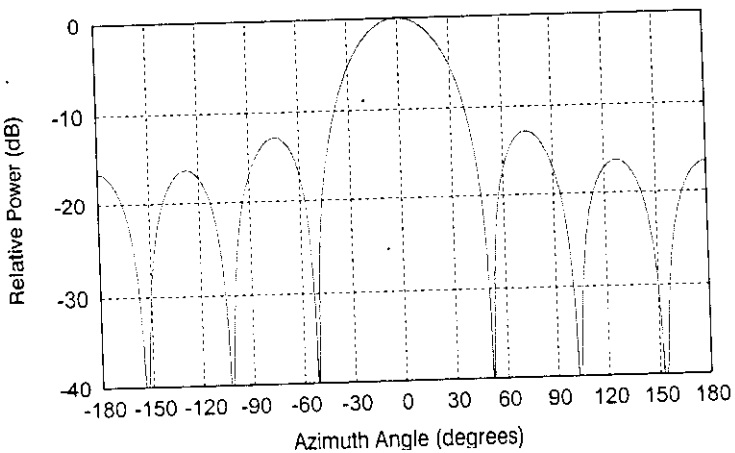

(a)

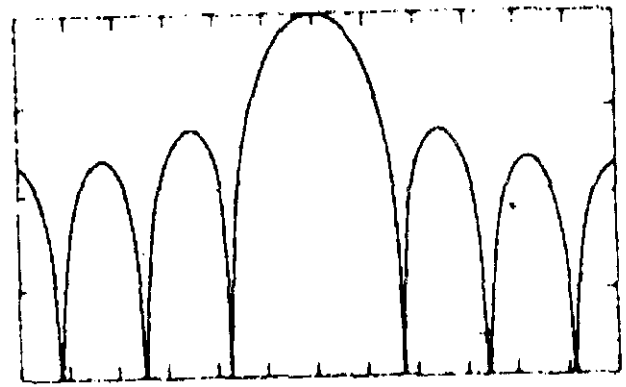

(b)

(iv) Mode –3 through +3 (Figure text given on page 26)

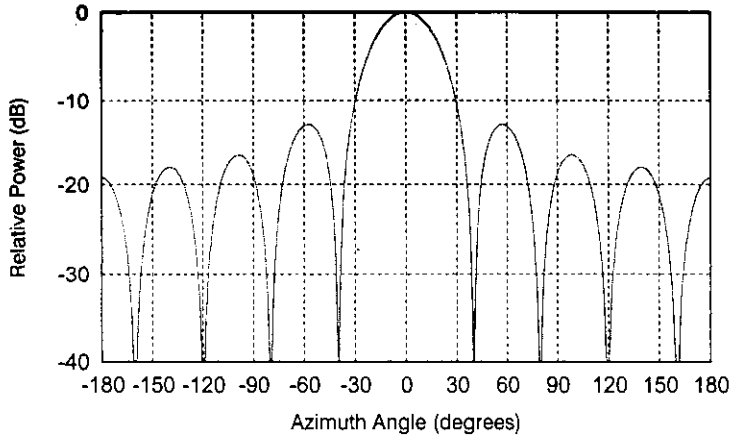

(a)

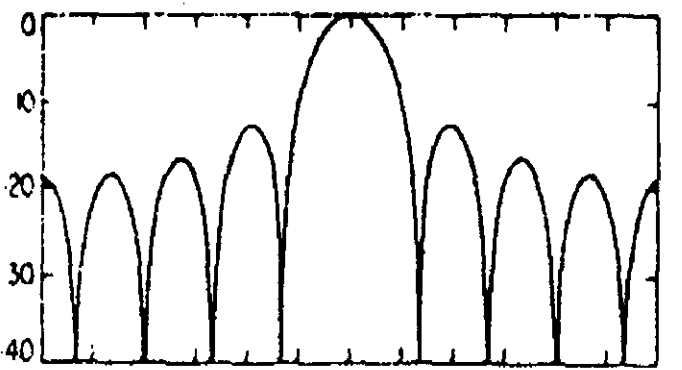

(b)

(v) Mode –4 through +4 (Figure text given on page 26)

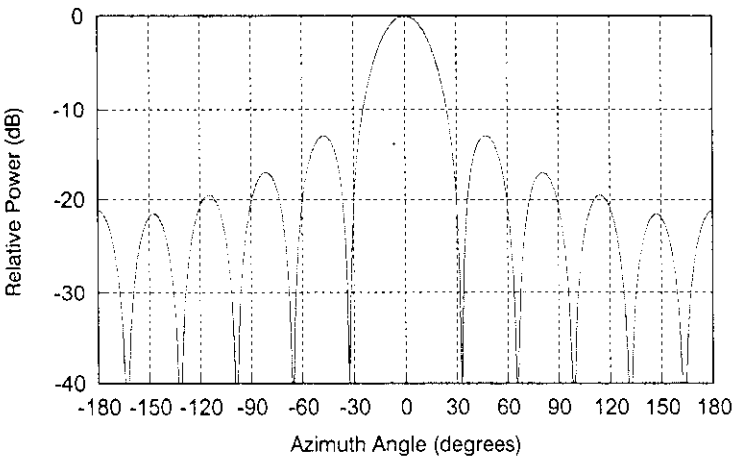

(a)

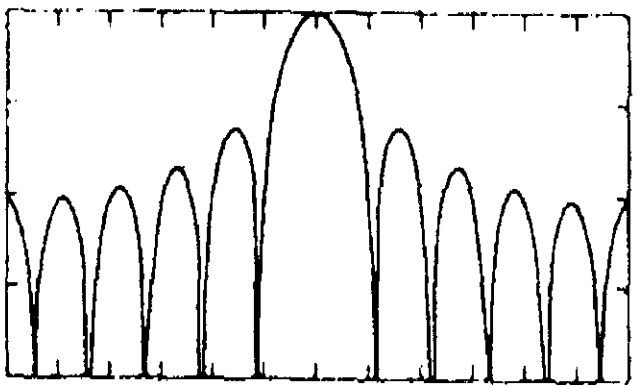

(b)

(vi) Mode –5 through +5 (Figure text given on page 26)

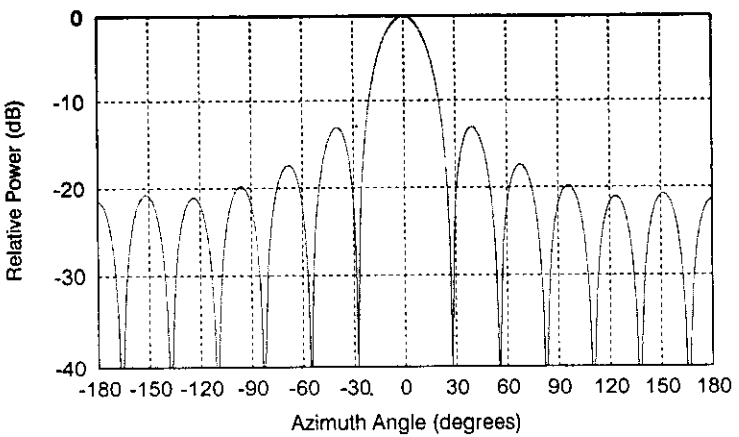

(a)

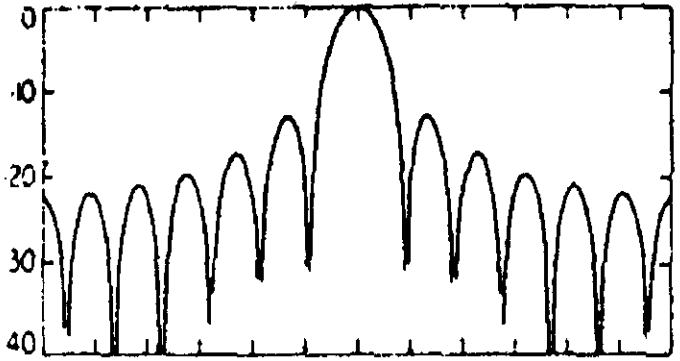

(b)

(vii) Mode –6 through +6 (Figure text given on page 26)

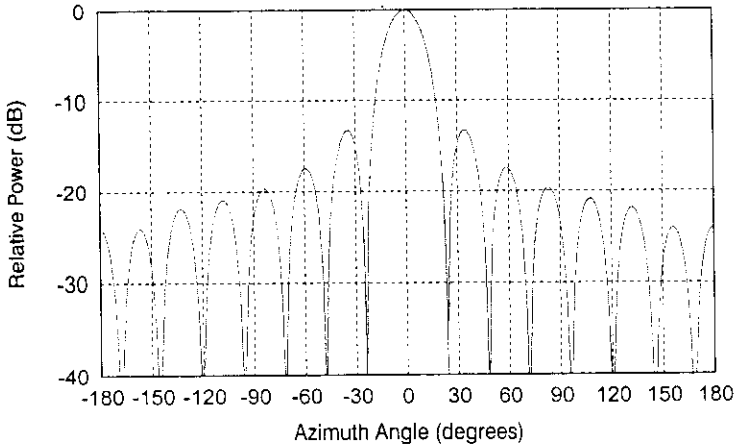

(a)

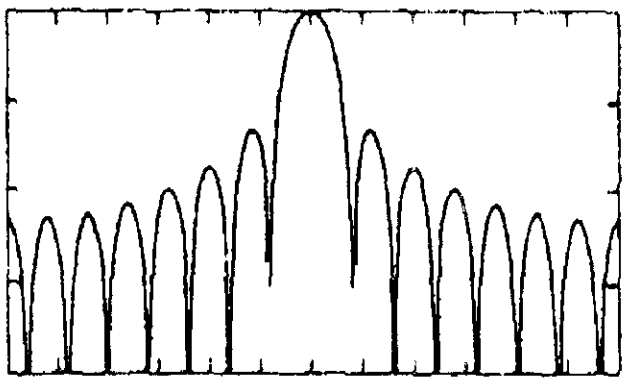

(b)

(viii) Mode –7 through +7 (Figure text given on page 26)

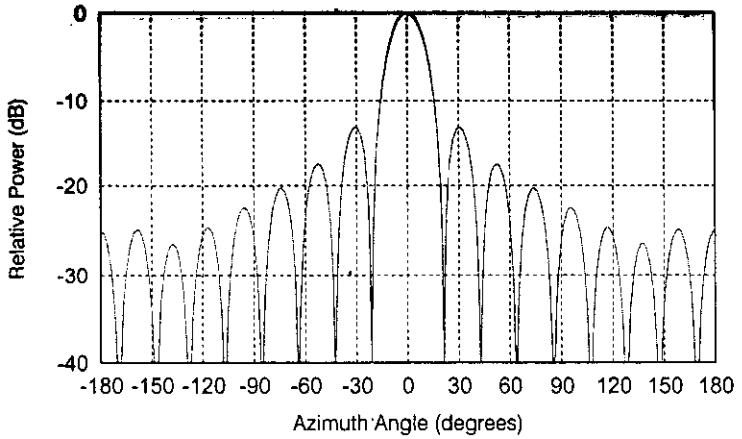

(a)

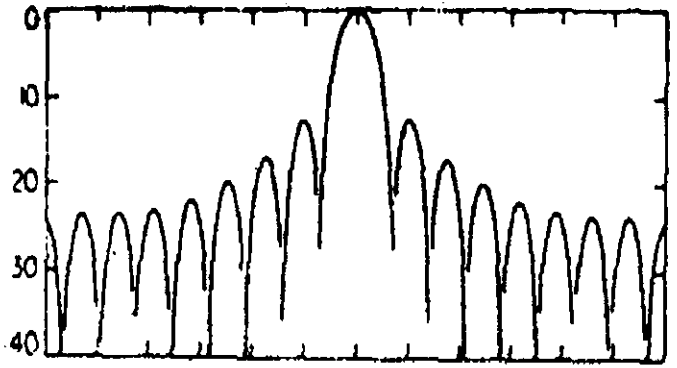

(b)

(ix) Mode –8 through +8 (Figure text given on page 26)

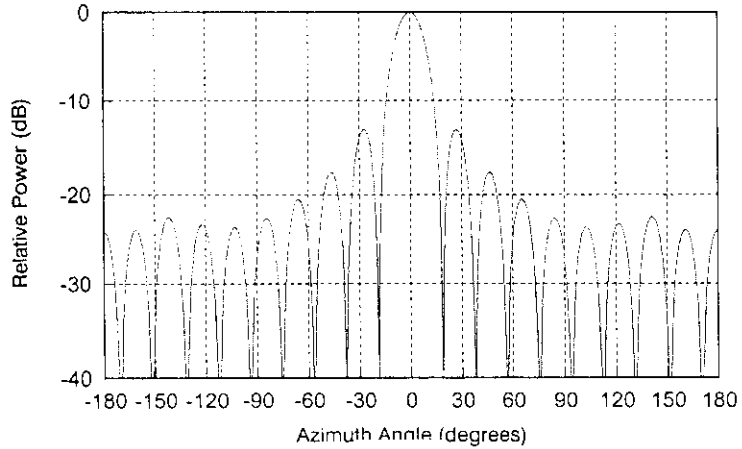

(a)

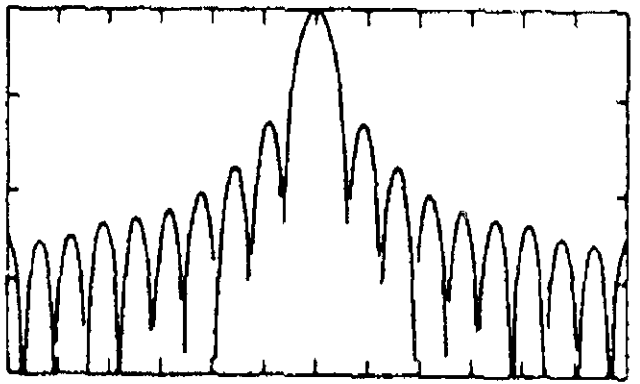

(b)

(x) Mode –9 through +9 (Figure text given on page 26)

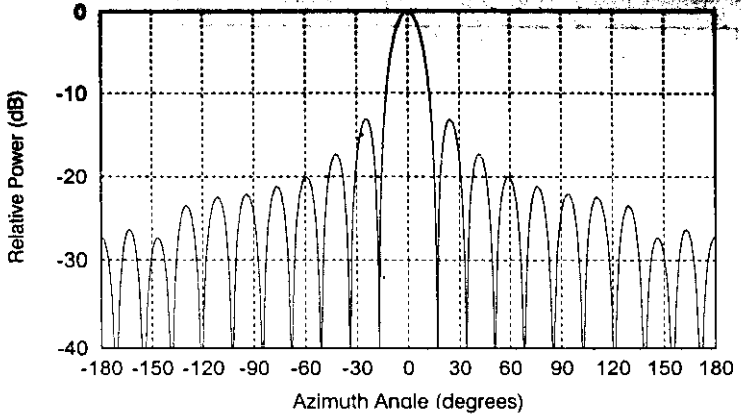

(a)

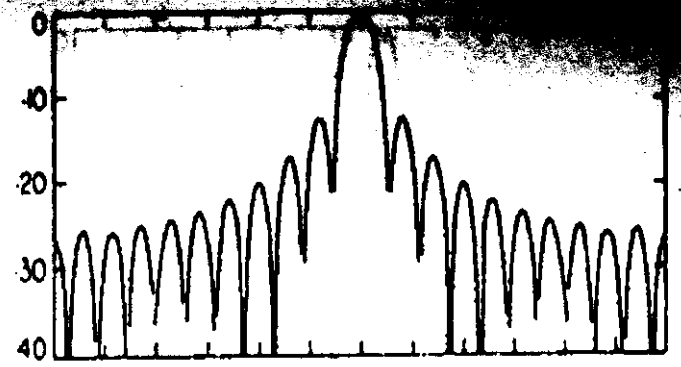

(b)

(xi) Mode –10 through +10 (Figure text given on page 26)

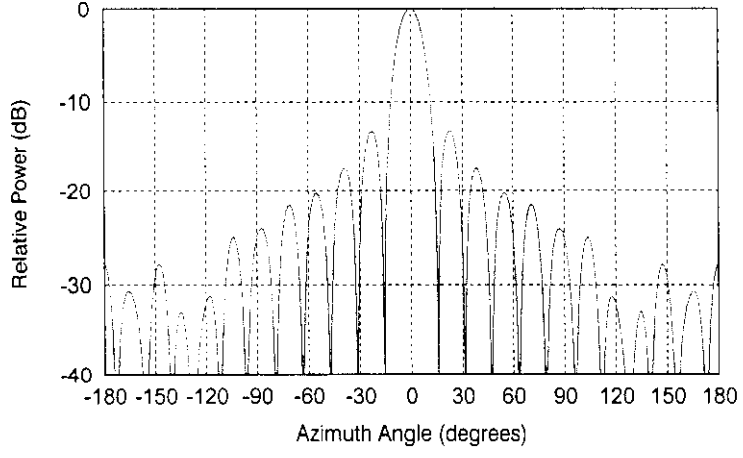

(a)

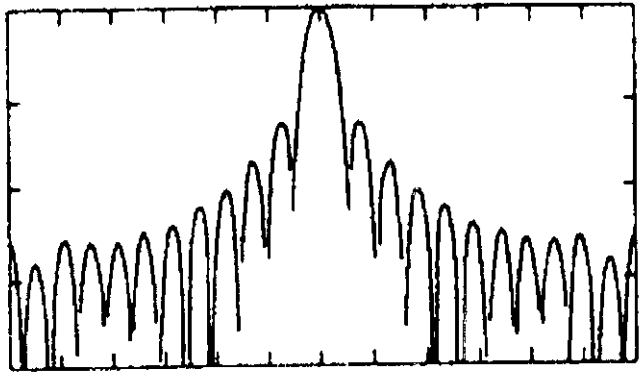

(b)

(xii) Mode –11 through +11 (Figure text given on page 26)

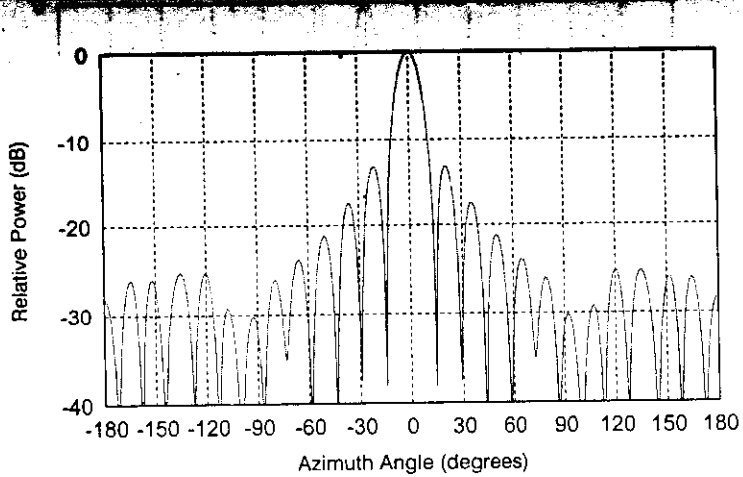

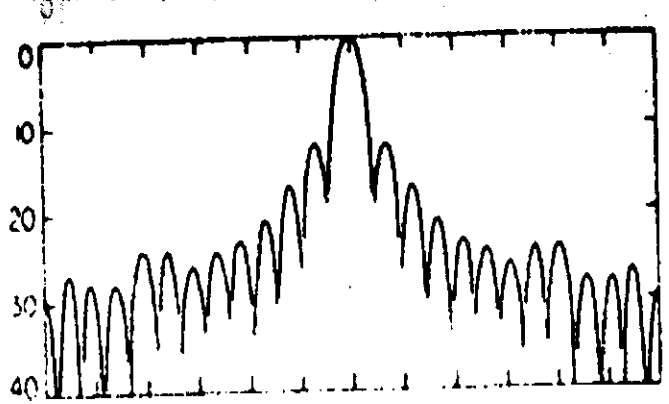

(a) (xiii) Mode –12 through +12 (Figure text given on page 26) (b)

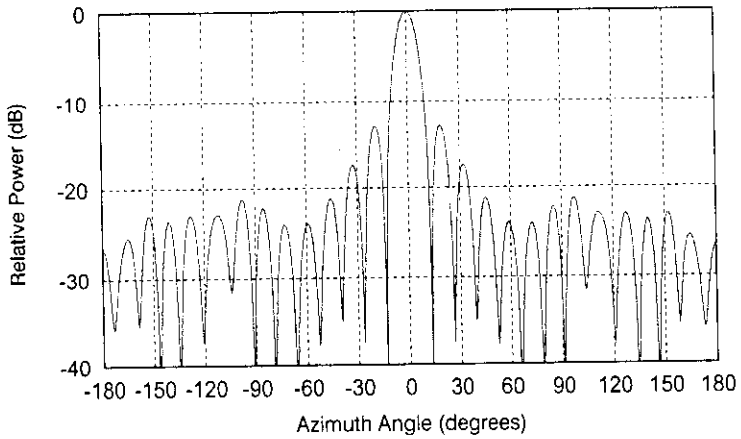

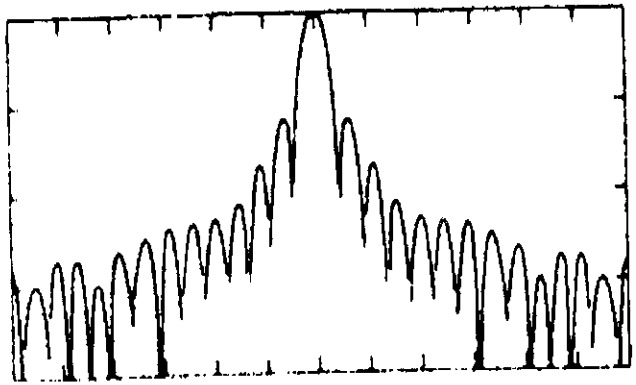

(a) (b)

(xiv) Mode –13 through +13 (Figure text given on page 26)

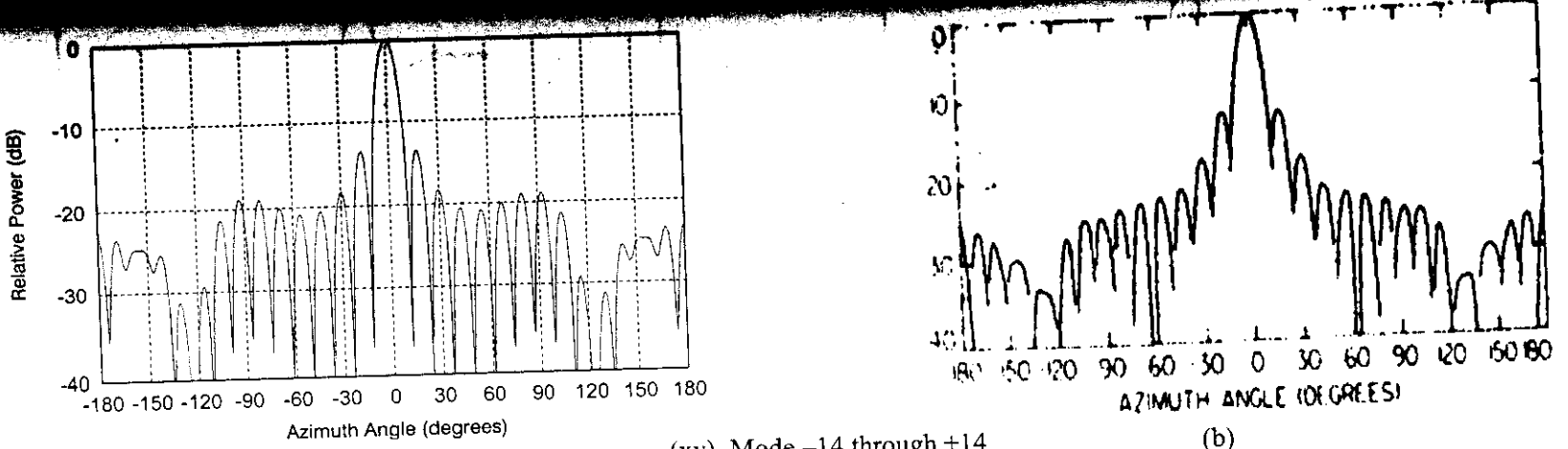

(a) (xv) Mode –14 through +14 (b)

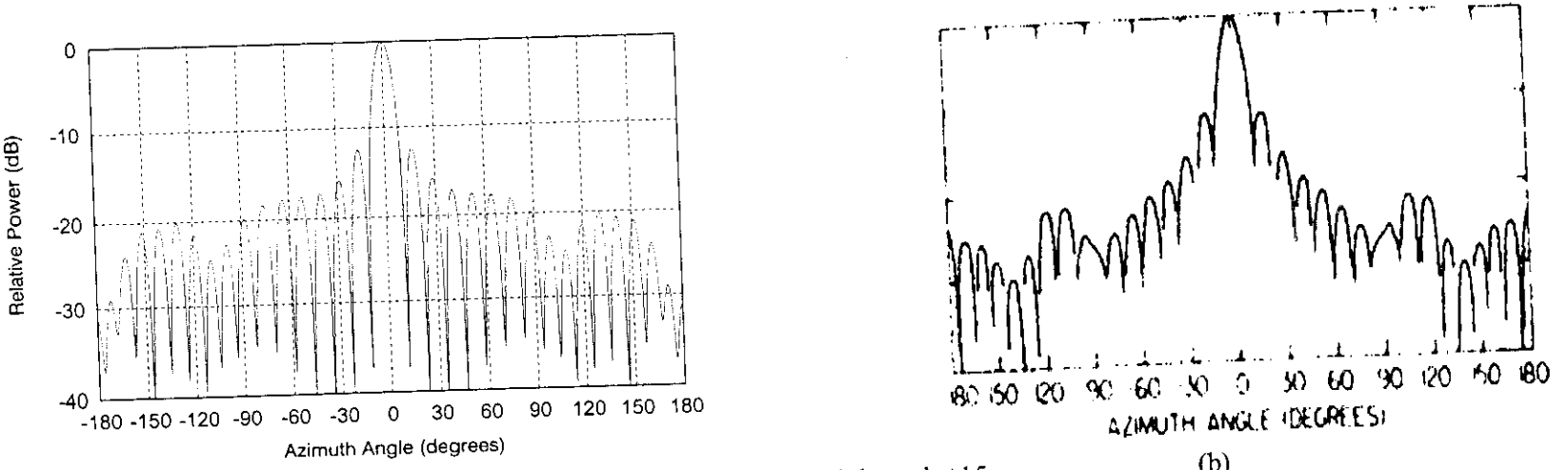

(a) (xvi) Mode –15 through +15 (b)

Figure 3.4 *Mode-by-mode buildup of the pattern* of a 32-element *circular array with uniform excitation* of the modes. (a) Computed plot (b) Reference plot (Sheleg 1968).

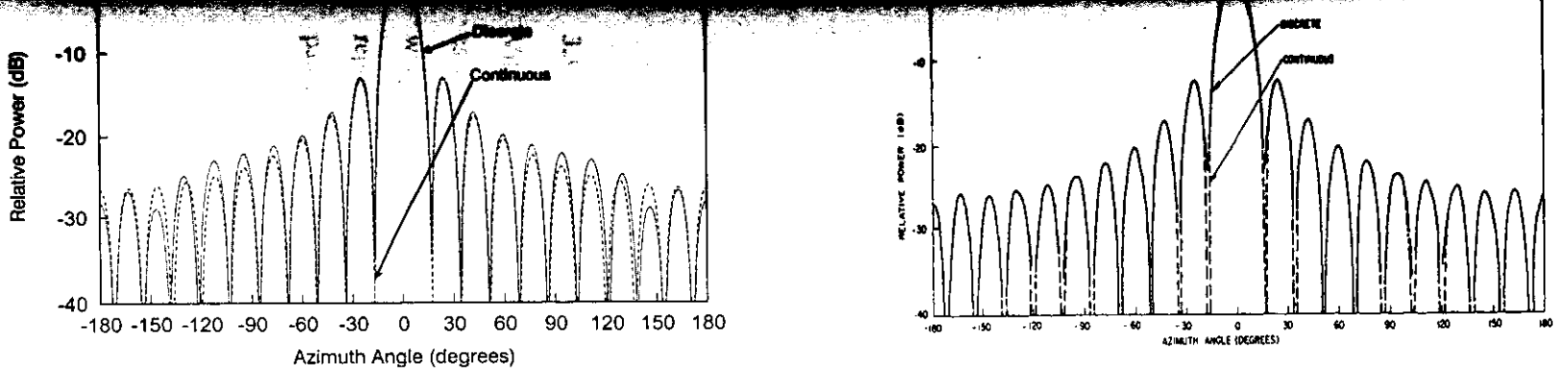

Figure 3.5 Comparison of the patterns of a 32-element *circular array* and of *continuous current sheet using 21 modes*. (a) Computed plot (b) Reference plot (Sheleg 1968).

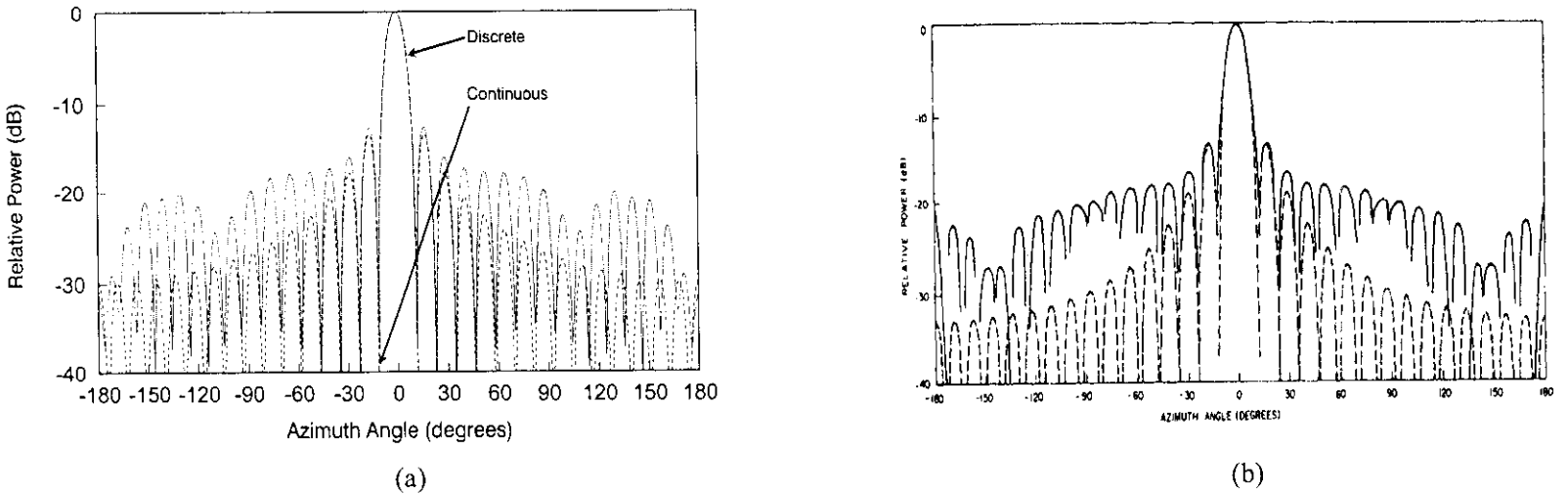

Figure 3.6 Comparison of the patterns of a 32-element *circular array* and of *continuous current sheet using 31 modes*. (a) Computed plot (b) Reference plot (Sheleg 1968).

It is well-known that the sidelobes from a linear array can be lowered by tapering the amplitude distribution over the array. By analogy, it should also be true for circular array if the mode amplitude distribution is tapered. Using phases from Table 3.1, simulations are performed for continuous current sheet using cosine taper and compared with the corresponding 32-element circular array pattern (B_K=cos($K\pi$/32)) using 31 modes (Fig. 3.7).

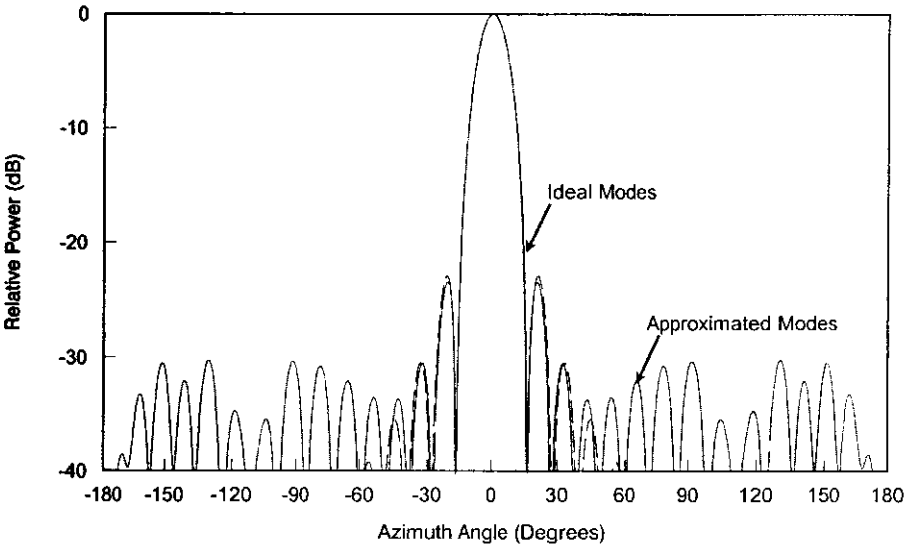

Figure 3.7 *Comparison* of the patterns of a 32-element *circular array* and of *continuous current sheet using cosine amplitude taper* on 31 modes.

3.3 Circular Arrays with Villeneuve Weighting

Villeneuve (1984) developed a technique of pattern synthesis for discrete arrays. It is essentially the combination of the best features of the uniform and Dolph-Chebyshev weightings. It involves the beam pattern synthesis initially with uniform weighting and then replacing the first $\bar{n}-1$ roots with modified Dolph-Chebyshev roots. The resulting beam pattern (Trees 2002) is given by

$$B_{\psi}(\psi)=\frac{\sin\left(\frac{N}{2}\psi\right)}{\sin\left(\frac{\psi}{2}\right)}\left[\frac{\prod_{n=1}^{\bar{n}-1}\sin\left(\frac{\psi-\psi_n'}{2}\right)\sin\left(\frac{\psi+\psi_n'}{2}\right)}{\prod_{n=1}^{\bar{n}-1}\sin\left(\frac{\psi-\psi_{un}}{2}\right)\sin\left(\frac{\psi+\psi_{un}}{2}\right)}\right] \tag{3.13}$$

The term inside the brackets modifies the beam pattern of the uniform weighting. The roots of the uniform weighting are $\psi_{un} = \frac{2\pi n}{N}$, $n = 1,2,\ldots, \bar{n}-1$. The numerator of the bracketed term is the set of the modified Chebyshev roots corresponding to the first $\bar{n}-1$ interior sidelobes. The denominator term is the corresponding set of the uniform weighting. The modified Chebyshev roots are used in order to avoid the discontinuity at $n = \bar{n}$.

The Dolph-Chebyshev pattern (Trees 2002) for an array with $N = 2M+1$ elements is expressed as

$$B_w(\psi) = e^{jM\psi} 4^M \prod_{p=1}^{M} \sin\left(\frac{\psi - \psi_p}{2}\right) \sin\left(\frac{\psi - \psi_p}{2}\right) \tag{3.14}$$

where, the roots are given by

$$\psi_p = 2\cos^{-1}\left(\frac{1}{x_0}\cos(2p-1)\frac{\pi}{4M}\right), \qquad p = 1, \ldots, 2M \tag{3.15}$$

The magnitude of the mainlobe corresponds the value of x_o,

$$x_o = \cosh\left(\frac{1}{N-1}\cosh^{-1} R_L\right) \tag{3.16}$$

where, R_L is the sidelobe ratio with respect to the mainlobe.

The modified Chebyshev roots are determined by using eqs (3.15) and (3.16). It is multiplied with $\sigma = \frac{2\pi\bar{n}}{N\psi_{\bar{n}}}$, where, $\psi_{\bar{n}}$ is the $\bar{n}$ th Chebyshev root.

Thus, $\sigma = \dfrac{\pi\bar{n}}{N\cos^{-1}\left(\frac{1}{x_o}\cos\left[(2\bar{n}-1)\frac{\pi}{4M}\right]\right)}$ and $\psi_n' = \sigma\psi_n$, $n = 1,\ldots, \bar{n}-1$.

Figures 3.8 and 3.9 represent the beam patterns for a 21-element and 41-element linear array with -20 dB sidelobe level. It can be observed that the Villeneuve beam pattern is same as the discretized Taylor beam pattern. The plots are validated against those available in literature (Trees 2002). If the number of antenna elements is N $\leq$11, some difference between the Taylor and Villeneuve beam patterns can be observed (Trees 2002). Moreover, the Villeneuve technique is preferred as compared to Taylor pattern.

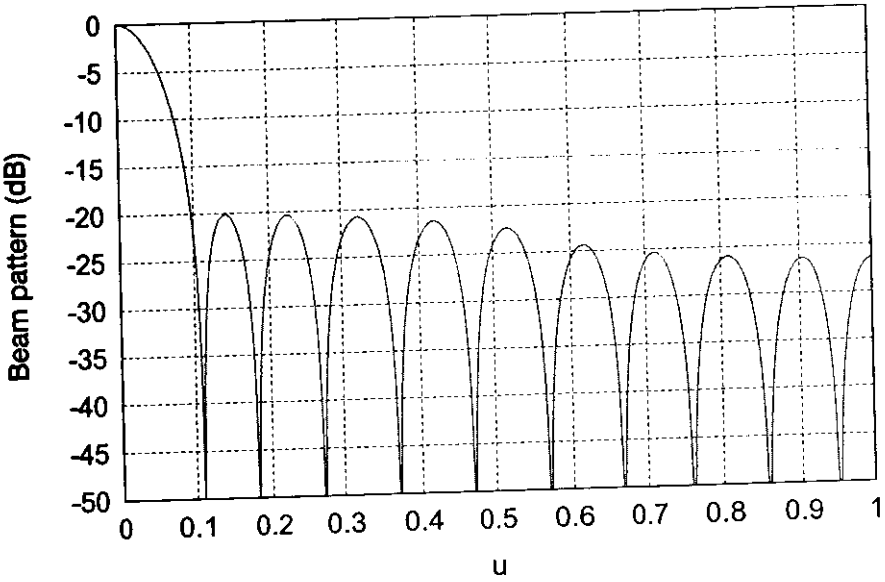
Beam pattern (dB)
0
-5
-10
-15
-20
-25
-30
-35
-40
-45
-50
0
0.1
0.2
0.3
0.4
0.5
0.6
0.7
0.8
0.9
1
u

(a)

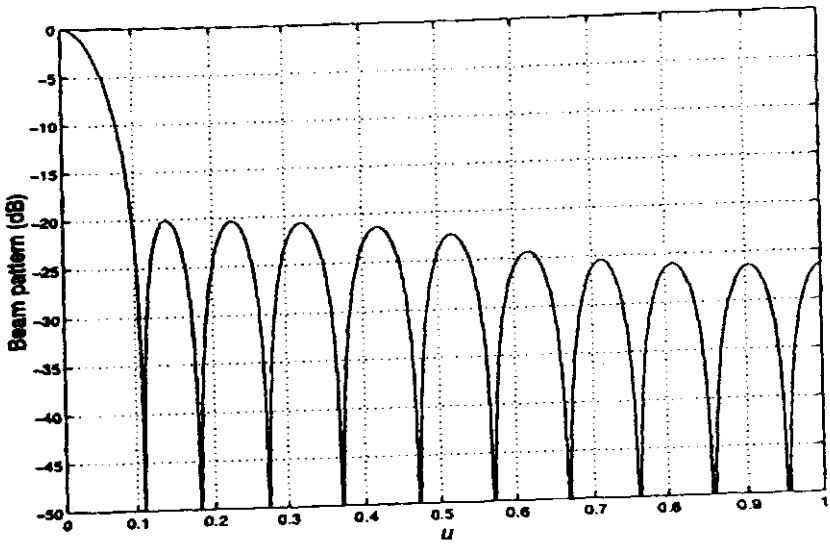
Beam pattern (dB)
u

(b)

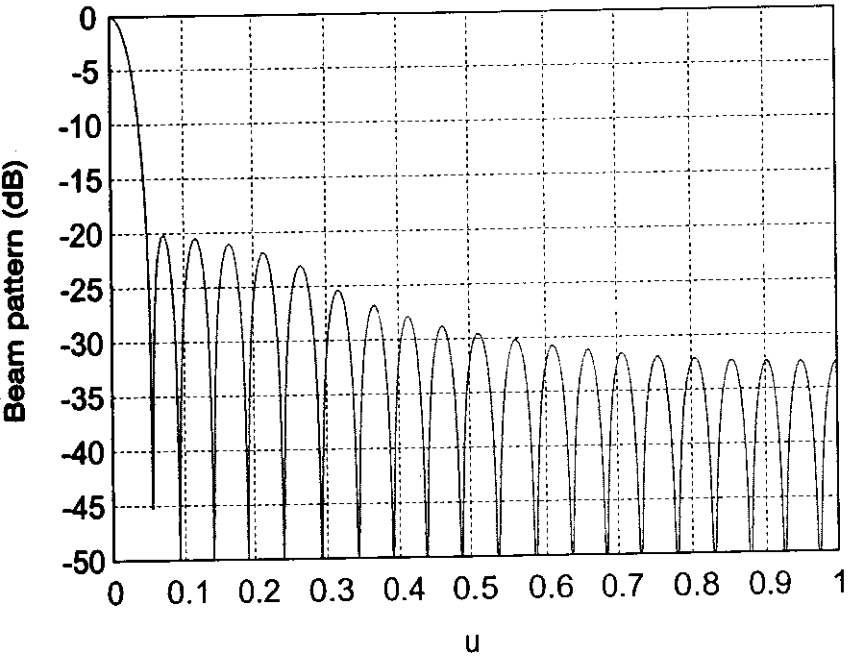
Beam pattern (dB)
0
-5
-10
-15
-20
-25
-30
-35
-40
-45
-50
0
0.1
0.2
0.3
0.4
0.5
0.6
0.7
0.8
0.9
1
u

(a)

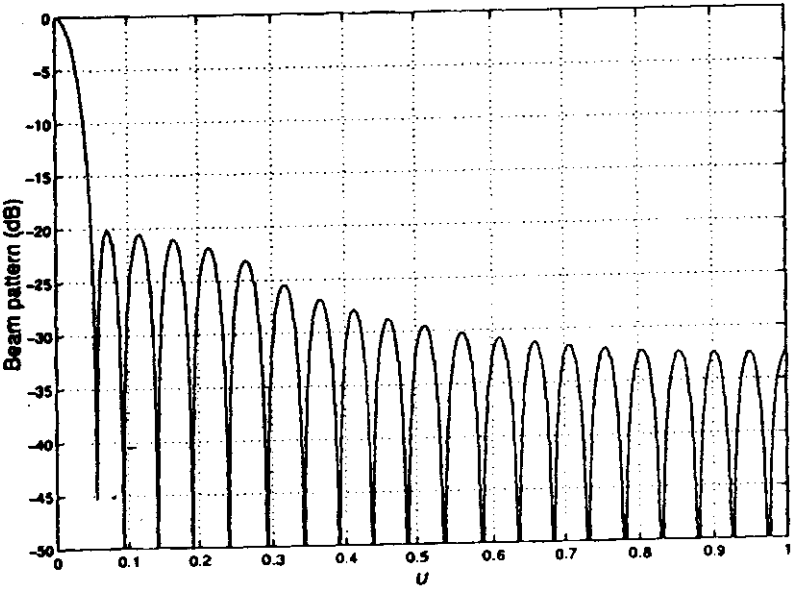
Beam pattern (dB)
0
-5
-10
-15
-20
-25
-30
-35
-40
-45
-50
0
0.1
0.2
0.3
0.4
0.5
0.6
0.7
0.8
0.9
1
u

(b)

are further extended for the circular array, whose elements are excited by distribution. The desired pattern is obtained using the expression

$$\left[w_{PM}^{H}\right]_m = \frac{\left[w_{VIL}^{H}\right]_m}{j^m J_m\left(2\pi R_\lambda\right)} \tag{3.17}$$

are the weights corresponding to the Villeneuve distribution, J_m is the Bessel with order. Since the highest spatial frequency that affects the beam pattern is $M \approx$ maximum limits of phase modes, $2M + 1$ can be used. Figure 3.10 shows the beam a 25-element circular array with radius $2\pi R = 10\lambda$. The 21-phase modes are for the pattern synthesis of circular array at $\theta = 90^{o}$. The sidelobe level of -20 dB on index $\bar{n} = 6$ are taken. Hence, the sidelobes are controlled up to sixth sidelobe which they start decaying gradually. Computed results are validated against that the literature (Trees 2002).

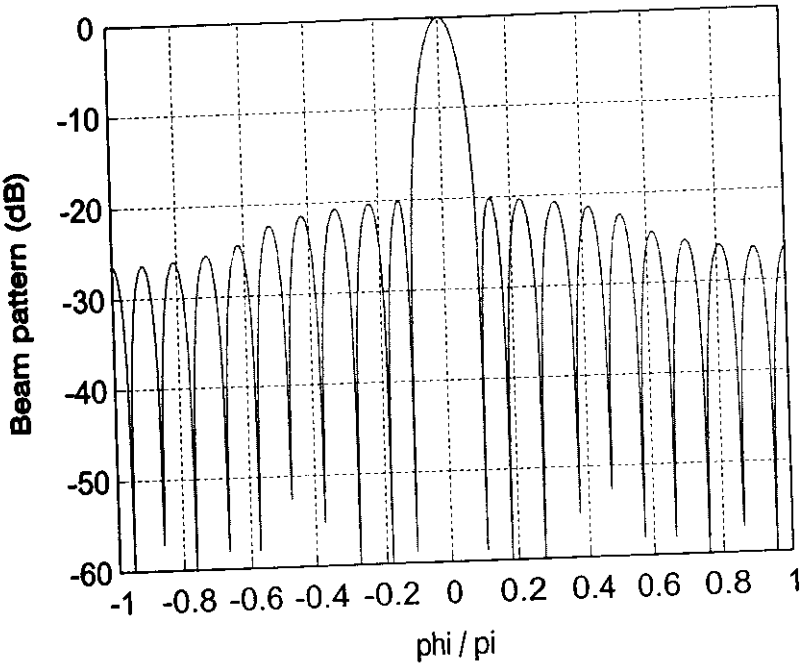
Beam pattern (dB)
0
-10
-20
-30
-40
-50
-60
-1
-0.8
-0.6
-0.4
-0.2
0
0.2
0.4
0.6
0.8
1
phi / pi

(a)

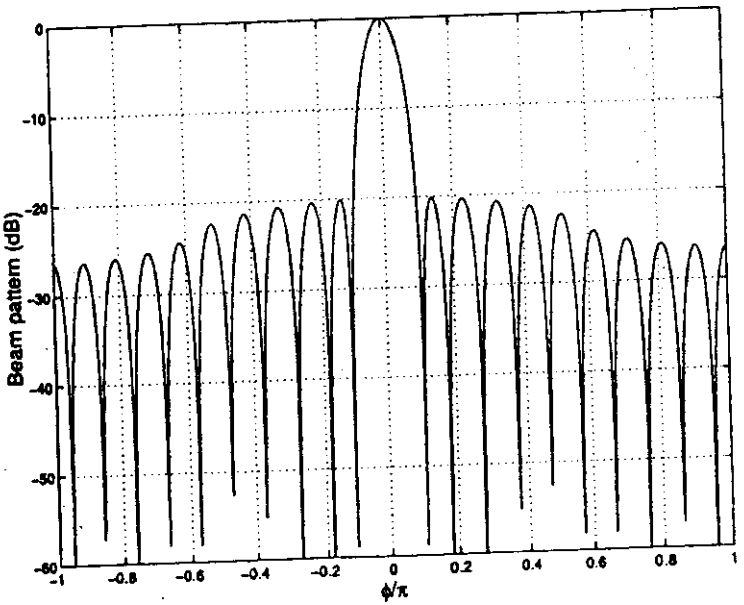
Beam pattern (dB)
0
-10
-20
-30
-40
-50
-60
-1
-0.8
-0.6
-0.4
-0.2
0
0.2
0.4
0.6
0.8
1
φ/π

(b)

4. Circular Sector Array

ircular sector array, consists of elements located over one-quarter (90°) of the **umference.** Circular sector arrays usually have sectoral ring of radiators mounted **trically on the** conducting cylinder (Fig. 4.1). The mainlobe of the radiation pattern is in **direction perpendicular** to the radiators and zero in endfire. The far-field contributed due **l elements** is evaluated over an angular range of 90°, i.e. ±45° *w.r.t.* the broadside.

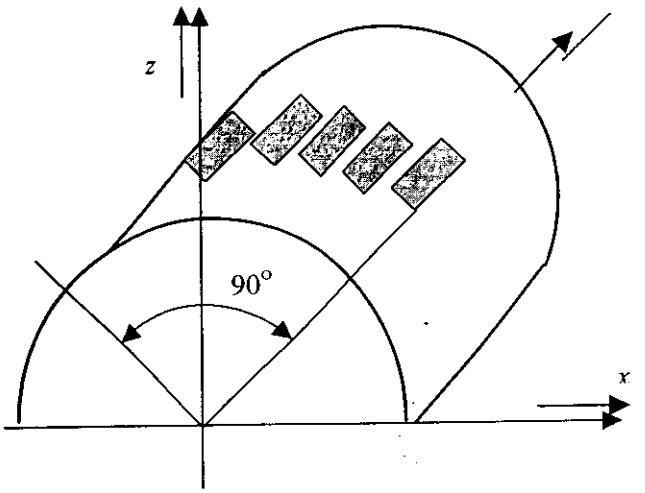

(a)

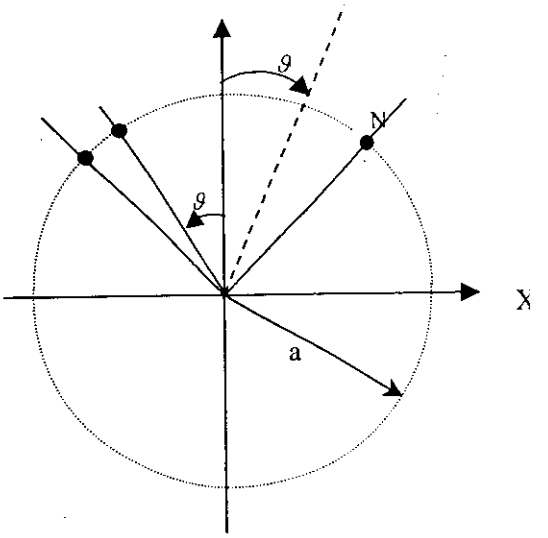

(b)

igure 4.1 Circular sector array antenna. (a) Layout of linear conformal array antenna, **b) Element positions.**

The voltage radiation pattern of the complete array is given by

$$S(\theta)=\sum_{i=1}^{N} S_{e_i}(\theta)e^{jk_0 r_i \hat{R}} = \sum_{i=1}^{N} S_{e_i}(\theta)e^{jk_0 a\cos(\theta-\theta_i)} \tag{4.1}$$

where $k_0 = \frac{2\pi}{\lambda}$ is the free space wavenumber and, r_i is the element position vector given by

$$r_i = \begin{pmatrix} x_i \\ y_i \\ z_i \end{pmatrix} = \begin{pmatrix} a\sin\theta_i \\ 0 \\ a\cos\theta_i \end{pmatrix}$$

here, a is the radius of the circle.

e unit direction vector $\hat{R}$ in the direction of observation θ is given by

$$= \begin{pmatrix} R_x \\ R_y \\ R_z \end{pmatrix} = \begin{pmatrix} \sin\theta\cos\phi \\ \sin\theta\sin\phi \\ \cos\phi \end{pmatrix}_{\phi=0} = \begin{pmatrix} \sin\theta \\ 0 \\ \cos\theta \end{pmatrix}$$

e element voltage radiation patterns, $S_{e_i}(\theta)$, $i = 1, 2, \ldots\ldots, N$, are given by

$$S_{e_i}(\theta) = \begin{cases} \cos(\theta-\theta_i) & for\ -\frac{\pi}{2}+\theta_i \le \theta \le \frac{\pi}{2}+\theta_i \\ 0 & elsewhere \end{cases} \tag{4.2}$$

ere $\theta_i = \frac{(2i-N-1)\pi}{4(N-1)}$,

uming that there are N elements, evenly distributed over the quarter circumference of the cular cylinder.

ures 4.2 through 4.5 illustrate the radiation pattern of a circular sector array antenna with ferent radius of the circle, *viz.* $\frac{7\lambda}{4\sqrt{2}}$, $\frac{7\lambda}{2\sqrt{2}}$, $\frac{7\lambda}{\sqrt{2}}$ and $\frac{35\lambda}{4\sqrt{2}}$ respectively. The patterns are aluated for $-45^\circ \le \theta \le 45^\circ$ using the formula $20\log\left(\frac{|S(\theta)|}{N}\right)$. All elements are equally itioned along the quarter of the circumference. The radii of the four conformal array ennas are chosen in such a way that the array antenna lengths, projected onto the x-axis $\frac{7\lambda}{4}$, $\frac{7\lambda}{2}$, 7λ and $\frac{35\lambda}{4}$ respectively.

If one compares these radiation patterns of curved array antennas for the given angular range with those of non-curved array antennas having the same number of antenna elements and the same projected lengths, the sidelobes of curved array antennas will have higher sidelobe level (Visser 2005).

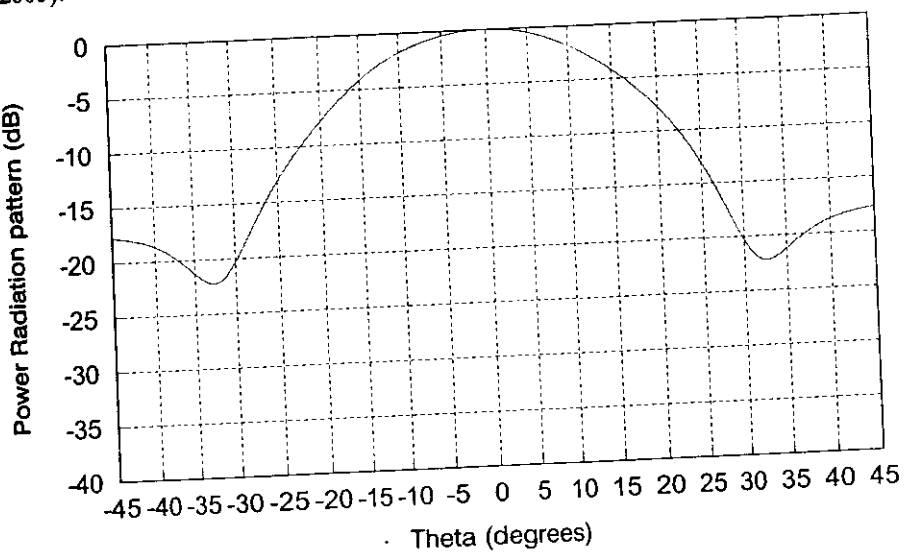

Figure 4.2 Power radiation pattern of 8-element, 90° *circular sector array antenna* for $a = \frac{7\lambda}{4\sqrt{2}}$.

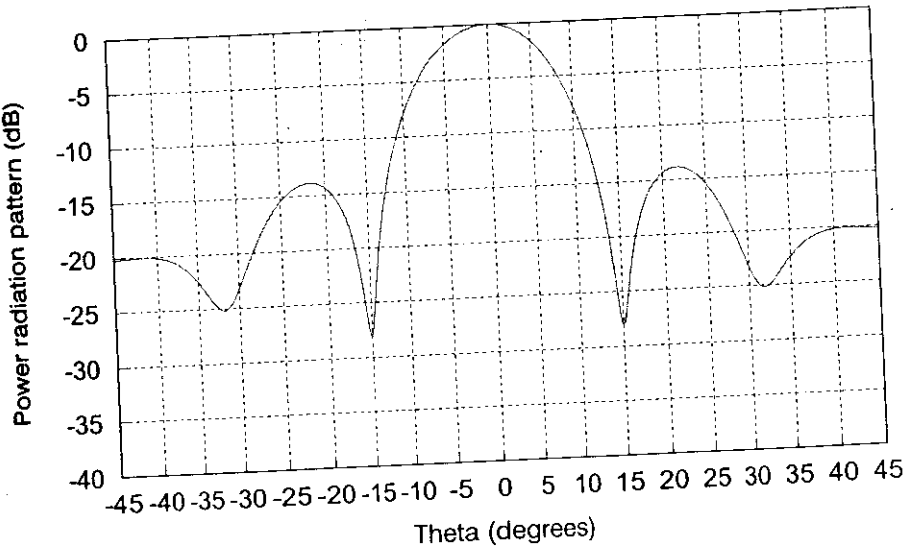

Figure 4.3 Power radiation pattern of 8-element, 90° *circular sector array antenna* for $a = \frac{7\lambda}{2\sqrt{2}}$.

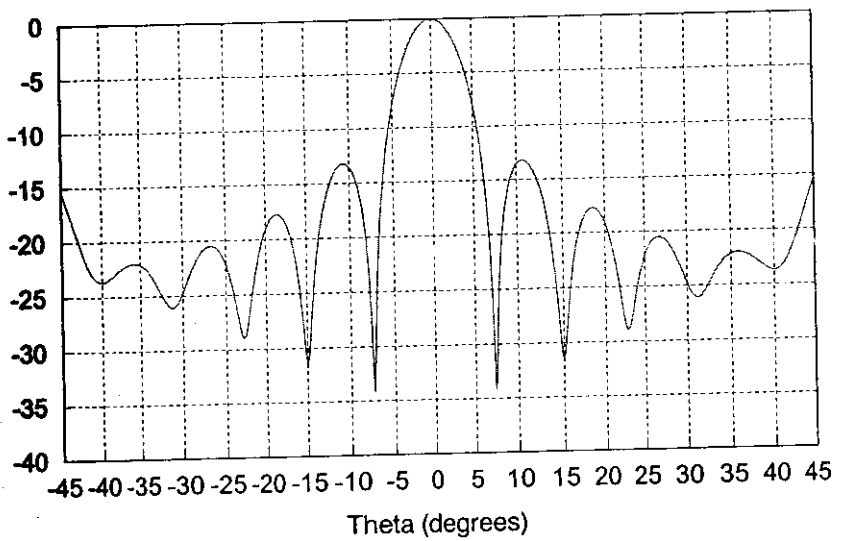

Figure 4.4 Power radiation pattern of 8-element, 90° *circular sector array antenna* for $a = \frac{7\lambda}{\sqrt{2}}$.

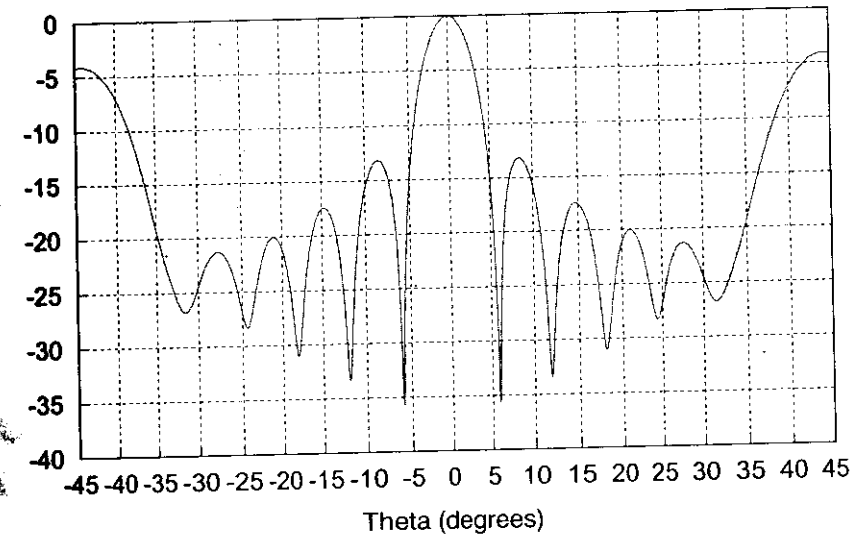

Figure 4.5 Power radiation pattern of 8-element, 90° *circular sector array antenna* for $a = \frac{35\lambda}{4\sqrt{2}}$.

Further beam is scanned in the x-z plane and the conformal phased array antenna is given by

$$S(\theta)=\sum_{i=1}^{N} S_{e_i}(\theta)e^{jk_0 a\cos(\theta-\theta_i)-\cos(\theta_0-\theta_i)} \tag{4.3}$$

where, θ_0 is the desired beam pointing direction.

For a beam scanned to the direction $\theta_0 = 30^\circ$, the conformal array antenna power radiation patterns for the two different radii $\frac{7\lambda}{\sqrt{2}}$ and $\frac{35\lambda}{4\sqrt{2}}$ are shown in Figs. 4.6 and 4.7 respectively. Figure 4.8 shows the power radiation pattern of 8-element and 16-element, 90° circular sector array antenna for the radius of circle a = $\frac{35\lambda}{4\sqrt{2}}$. It can be seen that the far sidelobes beyond ±30° are much higher in case of 8-element 90° circular sector array as compared to the 16-element array.

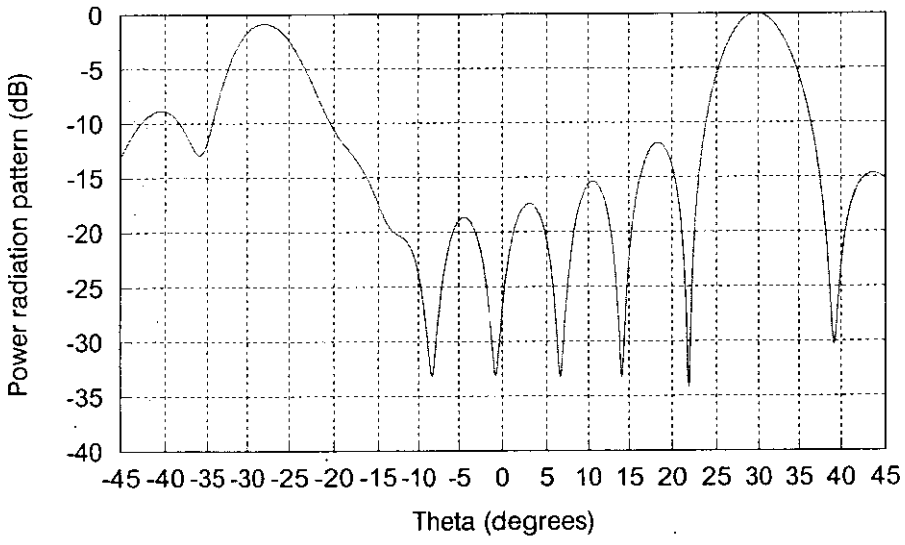

Figure 4.6 Power radiation pattern of 8-element, 90° *circular sector array antenna*, scanned to $\theta_o = 30^\circ$ for $a = \frac{7\lambda}{\sqrt{2}}$.

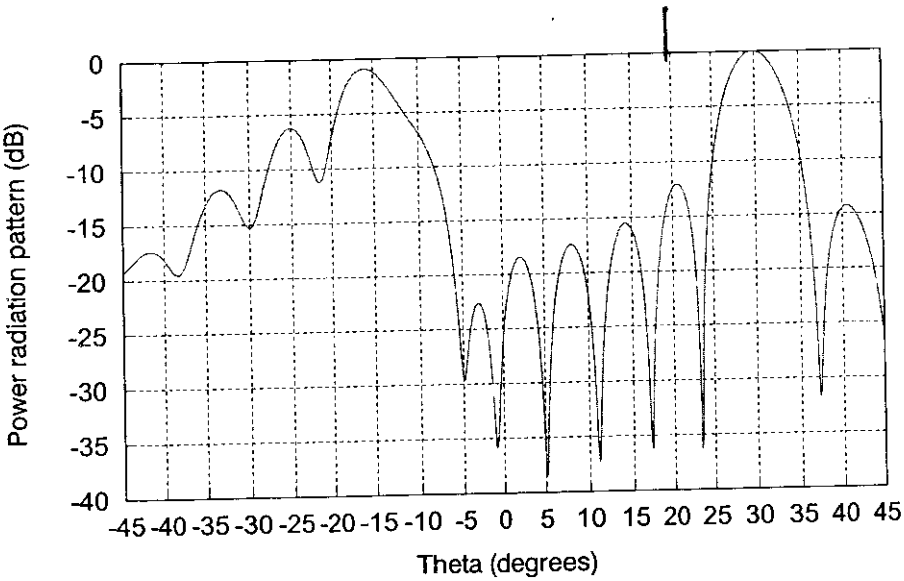

Figure 4.7 Power radiation pattern of 8-element, 90° *circular sector array antenna*, scanned to $\theta_o = 30°$ for $a = \frac{35\lambda}{4\sqrt{2}}$.

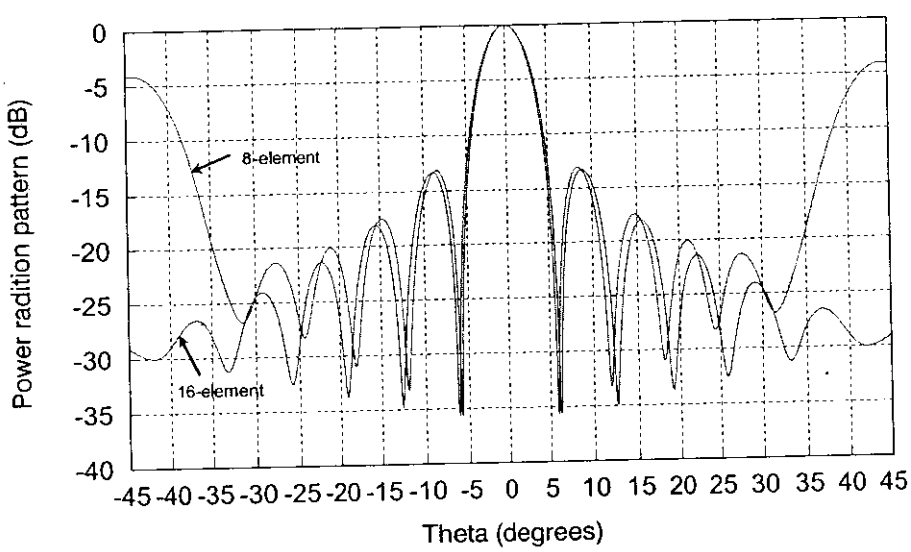

Figure 4.8 Power radiation pattern of 8-element and 16-element, 90° *circular sector array antenna* for $a = \frac{35\lambda}{4\sqrt{2}}$ and $\theta_o = 0°$.

5. Hexagonal Arrays

In hexagonal arrays, the elements are located on a hexagonal (or equilateral triangular) grid (Fig. 5.1). The vertical spacing between rows is $d_y = \frac{\sqrt{3}}{2} d_x$, where $d_x = \frac{\lambda}{2}$ is the horizontal inter-element spacing.

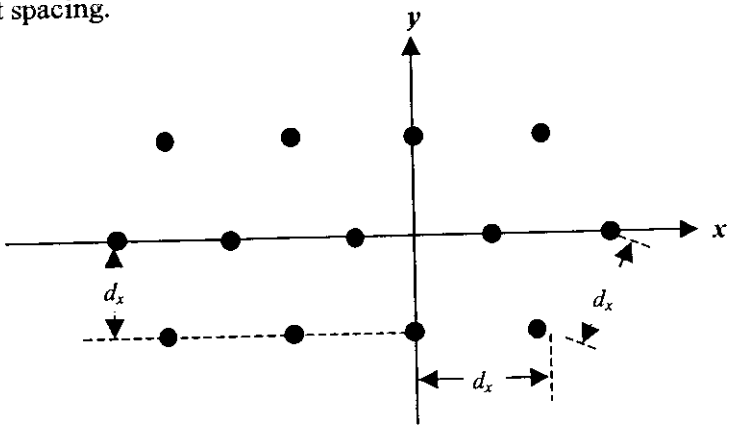

(a)

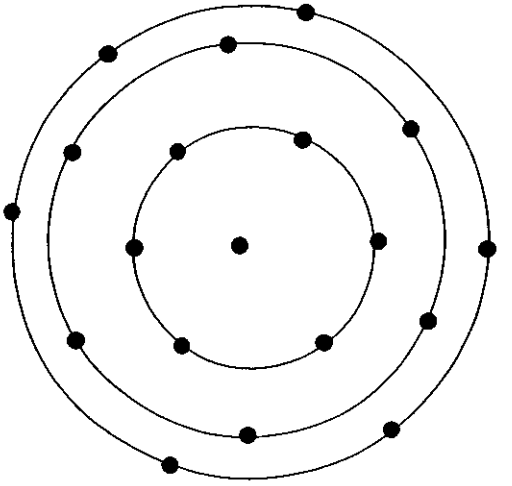

(b)

Figure 5.1 Configuration of a typical hexagonal array. (a) Element configuration, (b) Nineteen elements hexagonal array.

The reasons for this specific spatial distribution of the antenna elements are

1. This distribution samples the spatial field. Moreover it is the optimum sampling strategy (Trees 2002) for the signals that are band-limited over a circular region of Fourier plane.

2. If the beam is scanned inside a cone whose axis is normal to the array then less number of antenna elements (13.4% less) is required, which is preferred in view of the economical cost.

3. It is useful for all the desired beam patterns having circular symmetry.

In a standard hexagonal arrays (SHA), the total number of antenna elements is 7, 19, 37, 61,... according to the expression,

$$N_H = 1 + \sum_{n=1}^{N_x-1} 6n \tag{5.1}$$

where, N_x is the number of elements in the horizontal row through the origin. In general, N_x is a odd number in order to have a symmetric array.

The beam pattern is

$$B_u(u_x,u_y) = \sum_{m=-\frac{N_x-1}{2}}^{m=\frac{N_x-1}{2}} w^*_{nm} \exp\left\{ j\pi \left[m\frac{\sqrt{3}}{2}u_y - \frac{N_x-|m|-1}{2}u_x \right] \right\} \cdot \sum_{n=0}^{N_x-|m|-1} \exp\{j\pi n u_x\} \tag{5.2}$$

where, u_x and u_y are the direction cosines along x- and y-direction.

5.1 Uniform Weighting

For uniform weighting, the weights are given by

$$w_{nm} = \frac{1}{N_H} \tag{5.3}$$

The corresponding beam pattern for a hexagonal array is given by

$$B_u(u_x,u_y) = \frac{1}{N_H} \sum_{m=-\frac{N_x}{2}}^{\frac{N_x}{2}} \exp\left\{ j\pi \left[m\frac{\sqrt{3}}{2}u_y - \frac{N_x-|m|-1}{2}u_x \right] \right\} \cdot \sum_{n=0}^{N_x-|m|-1} \exp\{j\pi n u_x\} \tag{5.4}$$

Figures 5.2 show the beam pattern cuts ($\phi = 0^\circ$, $\phi = 10^\circ$, $\phi = 20^\circ$ and $\phi = 30^\circ$) of a standard 91-element hexagonal array with 11 elements in each horizontal row. The array is excited with the uniform weighting. On analyzing the distribution plots one can infer that the pattern is almost similar to the uniform distribution pattern for a linear array except that the sidelobes are at higher level. Results obtained are validated with those available in open literature (Trees 2002).

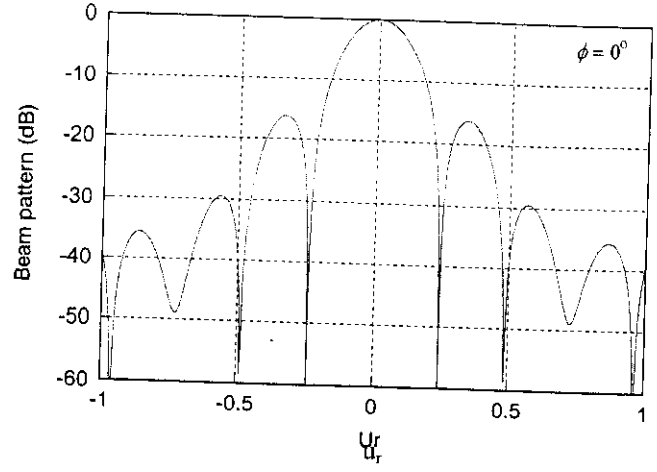

(a)

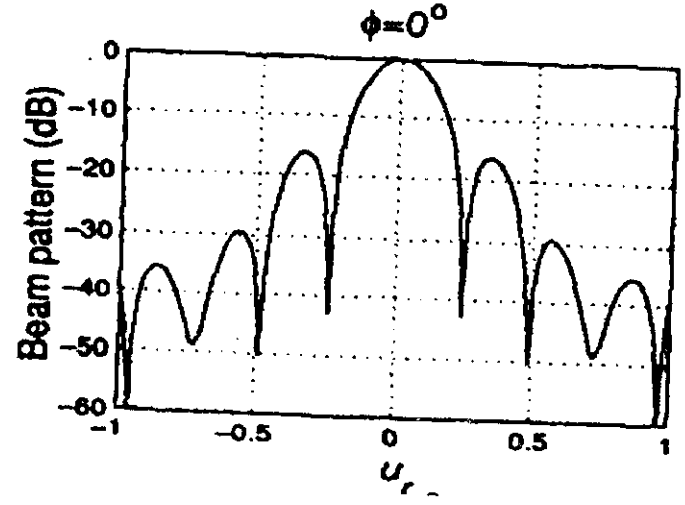

(b)

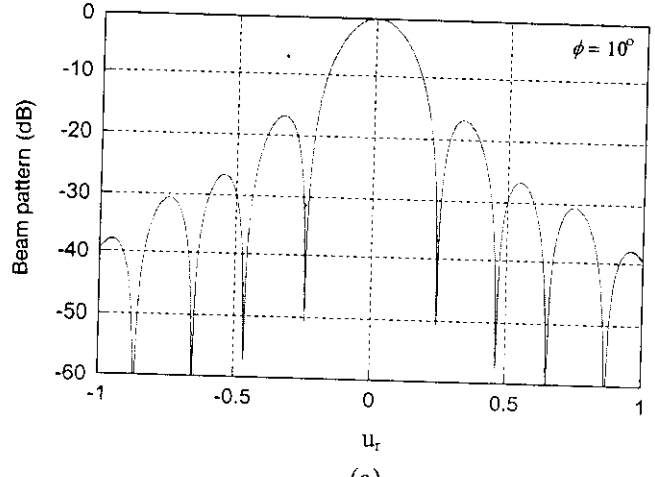

(a)

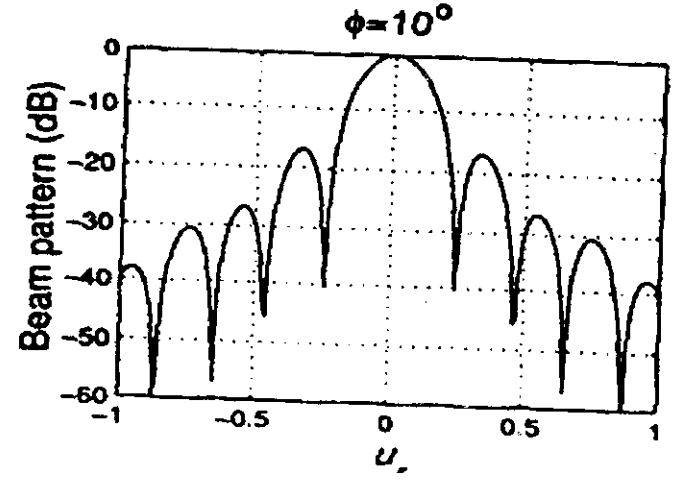

(b)

Figure 5.2a Validation plot for beam pattern cuts of a standard 91-element *hexagonal array with uniform weighting*: $\phi = 0^\circ$; $\phi = 10^\circ$. (a) Computed plot (b) Reference plot (Trees 2002).

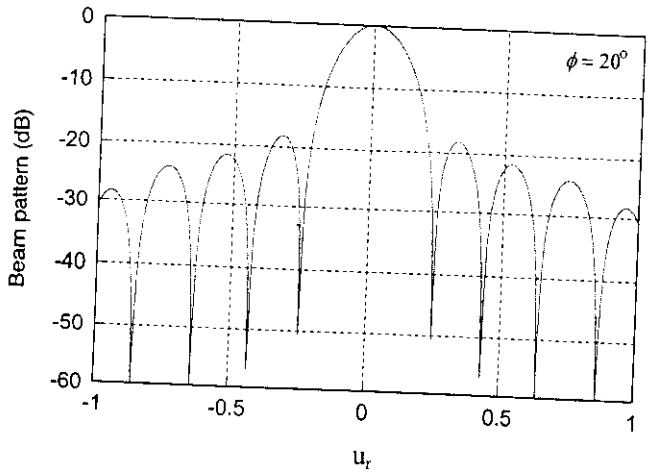

(a)

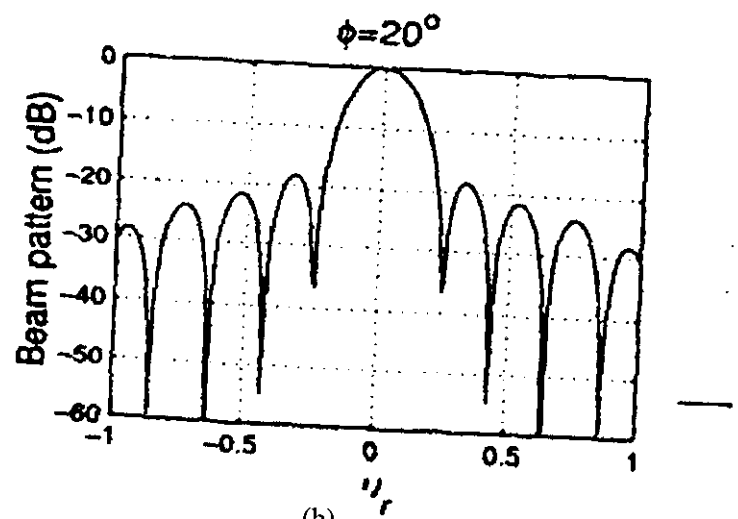

(b)

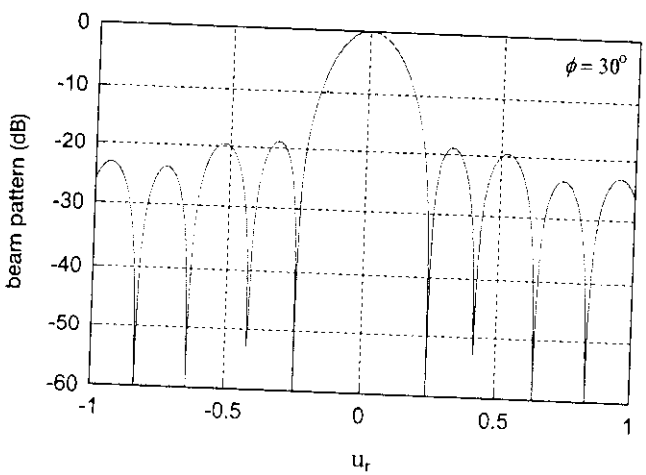

(a)

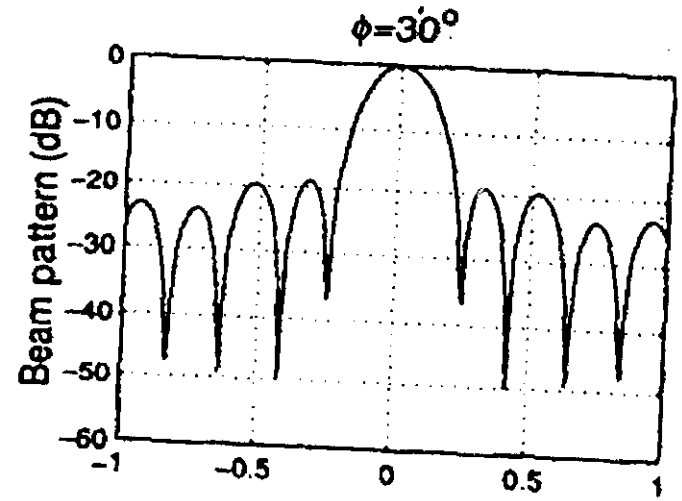

(b)

Figure 5.2b Validation plot for beam pattern cuts of a standard 91-element *hexagonal array with uniform weighting*: ϕ = 20°; ϕ = 30°. (a) Computed plot (b) Reference plot (Trees 2002).

5.2 Radial Taper Weighting

In order to reduce the sidelobe level of hexagonal array pattern with uniform distribution, radial tapering is incorporated in the weighting. The radial taper is given by

$$w_R(r) = 1 - \left(\frac{r}{R}\right)^2, \quad 0 \le r \le R \tag{5.5}$$

where, R is the radius of the continuous aperture. For radial taper weighting, the weights are given by

$$w_{nm} = 1 - \frac{\left(\left(n - \frac{N_x - |m| - 1}{2}\right)\frac{\lambda}{2}\right)^2 + \left(m\frac{\sqrt{3}}{4}\lambda\right)^2}{R^2} \tag{5.6}$$

Figures 5.3 present the beam pattern cuts ($\phi = 0°$, $\phi = 10°$, $\phi = 20°$ and $\phi = 30°$; $R = 2.75\lambda$) of a standard 91-element hexagonal array with radial taper weighting. It is apparent that the sidelobes are much lower and the mainlobe is wider as compared to the pattern of array with uniform weighting without any tapering. The computed results are validated against the literature (Trees 2002).

5.3 Radial Taper Squared Weighting

For further improving the sidelobe level and the mainlobe width, the radial taper squared weighting is incorporated. Thus,

$$w_R(r) = \left[1 - \left(\frac{r}{R}\right)^2\right]^2, \quad 0 \le r \le R \tag{5.7}$$

The corresponding weights are given by

$$w_{nm} = \left[1 - \frac{\left(\left(n - \frac{N_x - |m| - 1}{2}\right)\frac{\lambda}{2}\right)^2 + \left(m\frac{\sqrt{3}}{4}\lambda\right)^2}{R^2}\right]^2 \tag{5.8}$$

The beam pattern cuts ($\phi = 0°$, $\phi = 10°$, $\phi = 20°$ and $\phi = 30°$; $R = 2.75\lambda$) of a standard 91-element hexagonal array with radial taper squared weighting are shown in Fig. 5.4. The reduced mainlobe width and the sidelobe level are apparent. The computed plots are validated against the literature (Trees 2002).

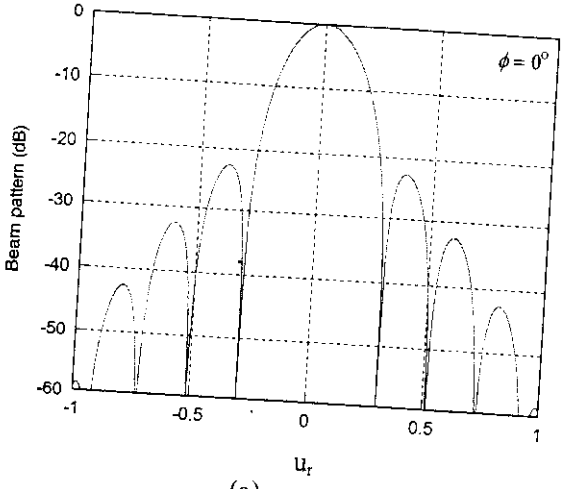

(a)

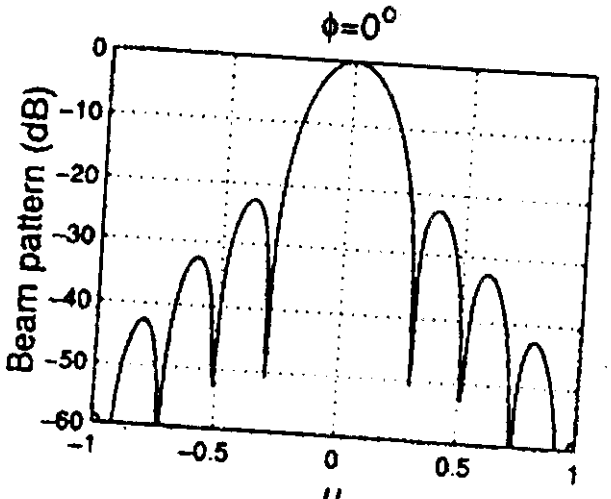

(b) u_r

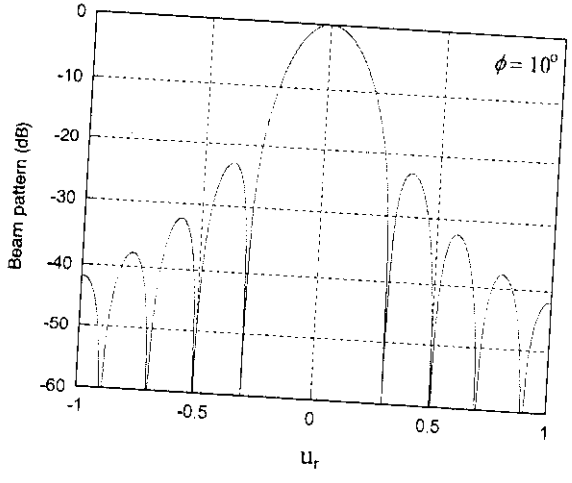

(a)

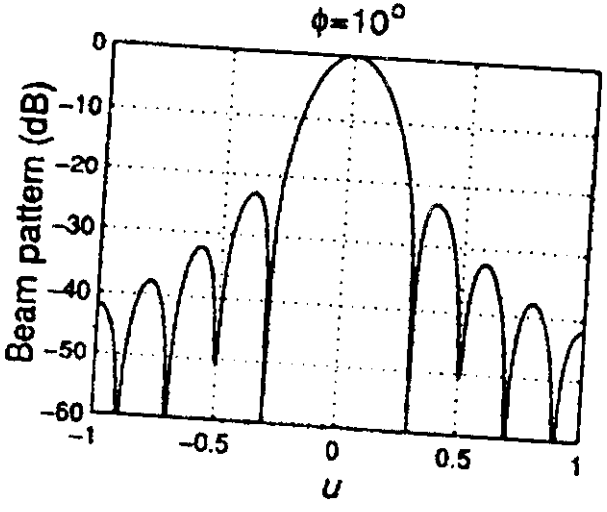

(b)

Figure 5.3a Validation plot for beam pattern cuts of a standard 91-element *hexagonal array with radial taper weighting* and the radius of continuous aperture R = 2.75λ: $\phi = 0°$; $\phi = 10°$. (a) Computed plot (b) Reference plot (Trees 2002).

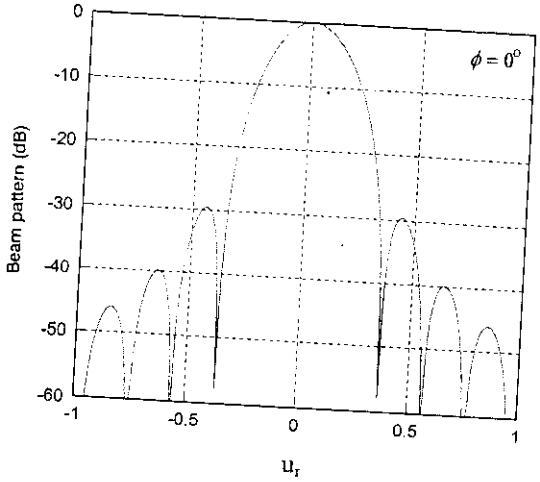

(a)

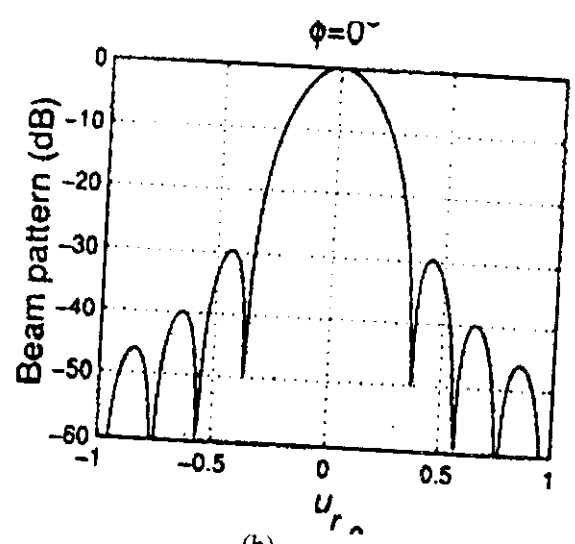

(b)

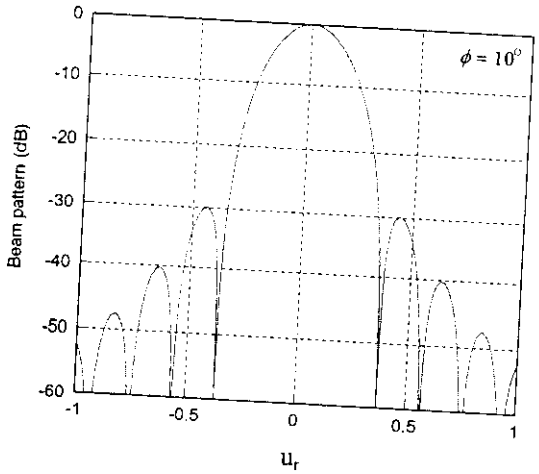

(a)

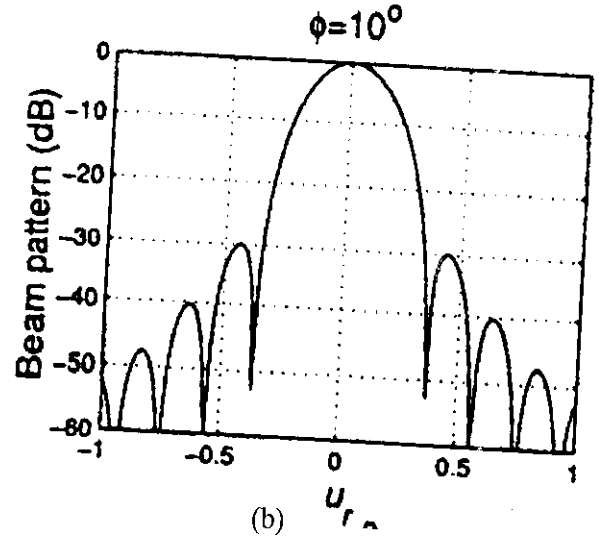

(b)

Figure 5.4a Validation plot for beam pattern cuts of a standard 91-element *hexagonal array* with *radial taper squared weighting* and the radius of continuous aperture R = 2.75λ: $\phi = 0^o$; $\phi = 10^o$. (a) Computed plot (b) Reference plot (Trees 2002).

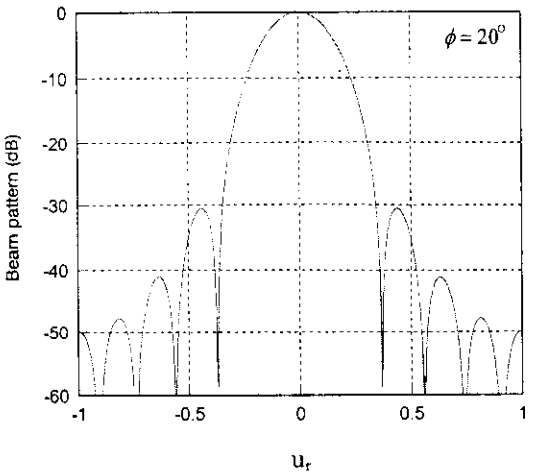

(a)

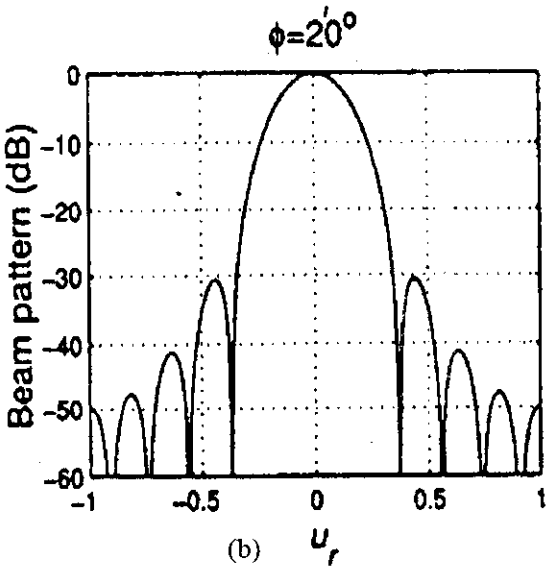

(b)

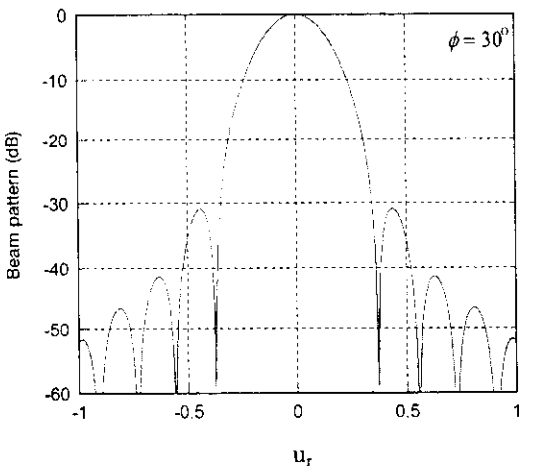

(a)

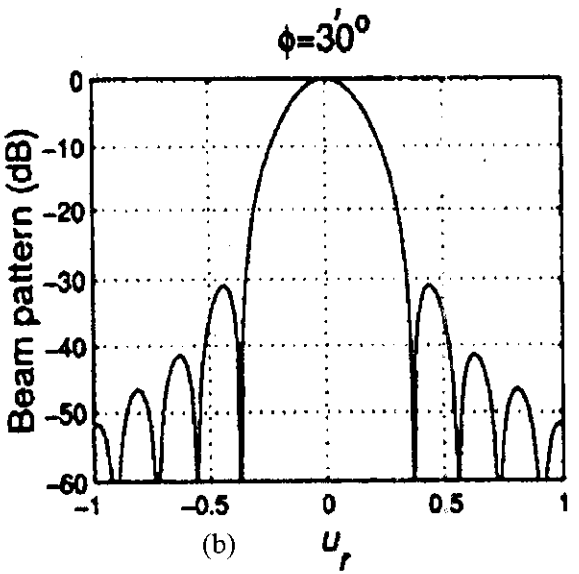

(b)

Figure 5.4b Validation plot for beam pattern cuts of a standard 91-element *hexagonal array* with *radial taper squared weighting* and the radius of continuous aperture R = 2.75λ: ϕ = 20°; ϕ = 30°. (a) Computed plot (b) Reference plot (Trees 2002).

6. Cylindrical Arrays

In many applications, the physical location of the sensors must conform to the shape of the curved surface where it is located on, e.g. arrays mounted on aircraft, missiles or submarines. These non-planar arrays are referred to as conformal arrays. The two commonly used conformal array geometries are cylindrical and spherical.

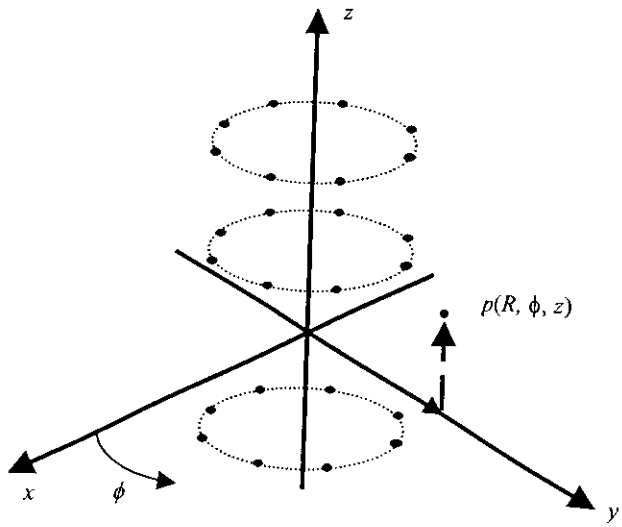

Figure 6.1 Cylindrical array geometry and the cylindrical coordinate system.

The beam pattern of the cylindrical array geometry (Fig. 6.1) is expressed as,

$$B(\theta,\phi) = \sum_{n=-\frac{N-1}{2}}^{\frac{N-1}{2}} e^{jk_0 z_n \cos\theta} \left\{ \sum_{m=1}^{M} w_{nm}^{*} e^{jk_0 R \sin\theta \cos(\phi-\phi_i)} \right\} \tag{6.1}$$

where, N is the number of circular arrays and M is the number of elements in each circular array. The centre of the circular arrays is the z-axis and the array is symmetric in the z-direction about the origin. If w_{nm} is separable, $w_{nm}^{*} = w_n^{*} w_m^{*}$, where w_n and w_m are the weights corresponding to the linear and circular arrays respectively.

The beam pattern can then be reduced to (Trees 2002)

$$B(\theta,\phi) = \sum_{n=-\frac{N-1}{2}}^{\frac{N-1}{2}} w_n^{*} e^{jk_0 z_n \cos\theta} B_{cir}(\theta,\phi) \tag{6.2}$$

or

$$B(\theta,\phi) = B_{lin}(\theta,\phi) B_{cir}(\theta,\phi) \tag{6.3}$$

Figure 6.2 illustrates the cylindrical array beam pattern at $\phi = 0$. It is assumed that the cylindrical array consists of 11 circular arrays with radius $2\pi R = 10\lambda$. Each circular array consists of 25-elements fed by the Villeneuve uniform phase mode excitation. Simulations are performed using 21-phase modes. The linear elements of circular arrays in the z-direction is excited by Dolph-Chebyshev weighting.

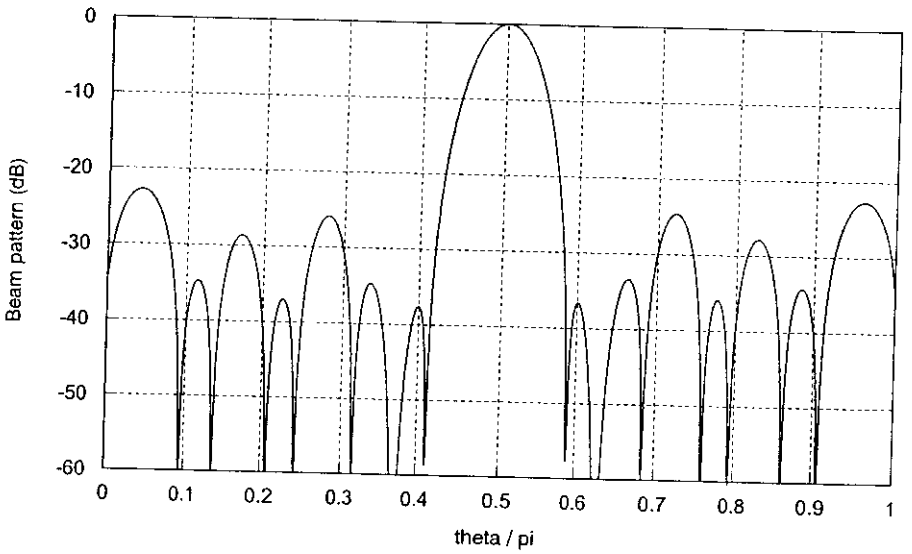

Figure 6.2 Beam pattern (at $\phi = 0^{\circ}$) of a *cylindrical array* consisting of 11 circular arrays with *Dolph-Chebyshev weighting*; Each circular array has 25-elements fed by *Villeneuve phase mode excitation*.

7. Summary

Conformal arrays are the most general type of phased array whose elements are mounted flush on a non-planar surface. They have applications in arrays for missiles, submarines, ships, high-speed aircraft, and also in systems that require wide-angle coverage. They generally belong to the class of non-linear arrays. Conformal antenna array on existing structure improves the aerodynamic or stealth characteristics vis-à-vis classical antenna. The present report presents the synthesized beam patterns of planar and non-planar arrays, *viz.* continuous circular aperture, circular arrays, circular sector arrays, hexagonal arrays and cylindrical arrays. The characteristics of different distributions like uniform, Villeneuve phase excitation, Taylor, and Dolph-Chebyshev weighting, used for the pattern synthesis of various conformal array geometries, are discussed.

The basic symmetry of circular and cylindrical arrays offers several advantages, which in addition to 360° scan angle, include an ability to compensate for the effects of mutual coupling by segregating the array excitation into a series of symmetrical spatial components. Further its directional patterns remain constant in shape over broad bandwidth.

The circular apertures provide the limiting case for most of the array configurations such as the concentric circular array and the hexagonal arrays. In circular array pattern, the mainlobe width is narrow as compared to a corresponding linear array of length equal to the diameter of the circle. The reduced beamwidth and more number of sidelobes are due to increased concentration of the elements at the sides of the circular aperture as compared to a linear array. Further the low sidelobes can be obtained by symmetrical amplitude taper on the front half of the circular array with zero or low excitation on the back of the array. Beam steering of the pattern can be achieved by electronic control of both amplitude and phase of each element.

Circular arrays are of particular importance because it provides a basic element of cylindrical arrays and even conical and spherical arrays, or arrays on generalized bodies of revolution. For a circular array with isotropic elements, the array weighting corresponds to sampling of the continuous aperture weighting. The mainlobe width of the pattern is not affected by increasing the number of elements in circular array.

The pattern characteristics of circular and cylindrical arrays cannot be expressed as the product of an element pattern and the array factor. This necessitates the consideration of the array patterns with directional elements. Moreover the mutual coupling between the elements

narrows the element pattern, so in practice, omnidirectional elements cannot be designed. Although it is true for planar arrays, it is much more important in the case of conformal arrays. This is because all the elements in conformal arrays point in different directions. The interaction between widely separated omnidirectional elements results in narrowed pattern and very limited bandwidth. Thus, if the array is designed using elements that radiate primarily in the radial direction, or in some forward sector, the characteristics of circular array will be substantially different and the bandwidth will also be improved.

The Taylor pattern is the continuous equivalent of the discrete Dolph-Chebyshev array distribution. It offers the narrowest beamwidth for a given sidelobe ratio. The Villeneuve phase mode technique is discrete analogue of generalized Taylor $\bar{n}$-distribution, used for continuous line source synthesis. It is essentially a combination of the best features of the uniform and Dolph-Chebyshev weightings. It involves the beam pattern synthesis initially with uniform weighting and then replacing the first $\bar{n}-1$ roots with modified Dolph-Chebyshev roots. When this distribution is expressed as a Fourier series, in which each term represents a current mode uniform in amplitude but having a phase varying linearly with angle. The pattern modes are the Fourier components of the radiation pattern of the current distribution. The radiation pattern is the sum of the modes contribution made to the pattern of a circular array by its elements. The Villeneuve phase excitation is better than Taylor weighting for number of elements less than 11.

If one compares the radiation patterns of curved array antennas for the given angular range with those of non-curved array antennas having the same number of antenna elements and the same projected lengths, the sidelobes of curved array antennas will have higher sidelobe level.

References

Davies, D.E.N., "A transformation between the phasing techniques required for linear and circular aerial arrays," *IEE Proceedings*, vol. 112, pp. 2041-2045, Nov. 1965.

Drabowitch, S., Papiernik, A., Griffiths, H. D., Encinas, J., and Smith, B. L., *Modern Antennas*. Dordrecht, The Netherlands, Springer, 2005.

Hansen, R. C., "A one-parameter circular aperture distribution with narrow beamwidth and low sidelobes," *IEEE Transactions on Antennas and Propagation*, vol. AP-24, pp. 477-480, July 1976.

James, P. W., "Polar patterns of phase corrected circular arrays," *IEE Proceedings*, vol. 112, pp. 1839-1848, Oct. 1965.

Mailloux, R. J., *Phased Array Antenna Handbook*. Norwood, MA, Artech House, 2005.

Rudge, A.W., Milne, K., Olver, A.D., and Knight, P., *The Handbook of Antenna Design*. vol. 2, London, Peter Peregrinus Ltd, 1983.

Sheleg, B., "A matrix-fed circular array for continuous scanning," *Proc. IEEE*, vol. 56, pp. 2016-2027, Nov. 1968.

Taylor, T. T., "Design of circular apertures for narrow beamwidth and low sidelobes," *IRE Transactions on Antennas and Propagation*, vol. AP-8, pp. 17-22, Jan. 1960.

Trees, V. L. H., *Optimum Array Processing: Detection, Estimation, and Modulation Theory*. New York, John Wiley & Sons, 2002.

Villeneuve, A.T., "Taylor patterns for discrete arrays," *IEEE Transactions on Antennas and Propagation*, vol. AP-32, pp.1089-1100, Oct. 1984.

Visser, H. J., *Arrays and Phased Array Antenna: Basics*. England, John Wiley & Sons, 2005.

List of Symbols

Angle measured in vertical plane	J_m	Bessel function of mth order
Phase factor w.r.t. the origin	J_o	Bessel function of zero order
Free space wavelength	K	mode
Transition index	k_o	Wave number
Azimuth angle	L	Length of the aperture
Phase difference between the adjacent modes	M	Elements in each circular array
Phase difference at the nth element	N	Total number of elements in array
Aspect angle	N_H	Number of elements in standard hexagonal array
Electrical length	N_x	Number of elements in horizontal rows through the origin
x-component in ψ space	R	Radius of the circular aperture
y-component of ψ space	r	Radius of the circular array
Beam pointing direction	R_L	Sidelobe ratio
Angle measured from broadside	$S(\theta)$	Voltage radiation pattern
Radius of the circular sector	$S_{ei}(\theta)$	Element voltage radiation pattern
Pattern of a dipole infront of a cylinder	u	Direction cosine with respect to u-space
Beam pattern of Villeneuve weighting in ψ space	u_R	Direction cosine in visible region
	u_x	Direction cosine w.r.t. x
Beam pattern in θ space	u_y	Direction cosine w.r.t. y
Beam pattern	w_n	Weights
Amplitude of modes	$[w_{PM}{}^H]$	Phase modes of circular Villeneuve excitation
Beam pattern in u space		
Phase mode coefficient	$[w_{VIL}{}^H]_m$	Phase modes of Villeneuve linear excitation
Directional pattern of circular array in elevation plane		
Spacing between the antenna elements		
Spacing between the x-axis elements in array		
Spacing between the y-axis elements in array		
Resultant pattern		
Element pattern		
Modified bessel function of first kind and order one		
$\sqrt{-1}$		
Bessel function of first order		